Alma Mater Studiorum
Università di Bologna

Department of Physics and Astronomy
Master Degree in Physics

Experimental evaluation of the z-resolution in different clinical Digital Breast Tomosynthesis systems using commercial phantoms.

Supervisor:
Prof. Maria Pia Morigi

Co-Supervisors:
Dr. Nicoletta Scrittori
Dr. Valentina Ravaglia

Presented by:
Sara Dalmonte

Academic year 2021/2022

Abstract

Digital Breast Tomosynthesis (DBT) is an advanced mammography technique based on the reconstruction of a pseudo-volumetric image. To date, image quality represents the most deficient section of DBT quality control protocols. In fact, related tests are not yet characterized by either action levels or typical values. This thesis work focuses on the evaluation of one aspect of image quality: the z-resolution. The latter is studied in terms of Artifact Spread Function (ASF), a function that describes the signal spread of a detail along the reconstructed focal planes. To quantify the ASF numerically, its Full Width at Half Maximum (FWHM) is calculated and used as a representative index of z-resolution. Experimental measurements were acquired in 24 DBT systems, of 7 different models, currently in use in 20 hospital facilities in Italy. The analysis, performed on the clinical reconstructed images, of 5 different commercial phantoms, lead to the identification of characteristic FWHM values for each type of DBT system. The ASF clearly showed a dependence on the size of the detail, providing higher FWHM values for larger objects. The z-resolution was found to be positively influenced by the acquisition angle: Fujifilm sistematically showed wider ASF profiles in ST mode (15°) than in HR mode (40°). However, no clear relationship was found between angular range and ASF, among different DBT systems, due to the influence of the peculiarities of each reconstruction algorithm. The experimental approach shown in this thesis work can be proposed as a z-resolution quality control test procedure. Contextually, the values found could be used as a starting point for identifying typical values to be included in the test, in a DBT protocol. Clearly, a statistically significant number of images is needed to do this. The equipment involved in this work is located in hospitals and is not available for research purposes, so only a limited amount of data was acquired and processed.

Contents

Introduction

Digital Breast Tomosynthesis (DBT) is an advanced mammography technique based on the reconstruction of a pseudo-volumetric image of the breast. This is achieved with specialized reconstruction algorithms that are able to combine the series of planar projections, of a compressed breast, acquired at different angles of the X-ray tube. This type of examination is able to limit the tissue overlap, typical of 2-dimensional mammography, which negatively affects the sensitivity and specificity with which normal fibroglandular tissues and abnormal lesions, i.e. microcalcifications, masses and spiculations, can be distinguished. Because of the limited acquisition angle, tomosynthesis is characterized by an anisotropic spatial resolution. In detail, the resolution in the planes parallel to the detector is better than that in the perpendicular direction, also called z-resolution. Despite this, to date the z-resolution is considered high enough to reduce the problem of tissue overlap.
In accordance with the current legislative decree, i.e. D.Lgs. 101/20 [2], and specific international European provisions, the Quality Control (QC) coordination of a mammography system, and all other radiological equipment, is mandatory for medical physicists. QC is part of quality assurance, which consists in all those planned and systematic actions necessary to provide adequate assurance that a system, component or procedure will perform satisfactorily in compliance with agreed standards. In detail, the medical physicist must perform QC according to the most recent guidelines which, for digital breast tomosynthesis, are EUREF 2018 [18] and ACR 2020 [19]. The quality control protocols for the 3-dimensional mammography are very recent and are still being optimized, in fact, many groups of experts around the world are still working on them [20-23]. Also in Italy, the Italian medical physicists belonging to AIFM (Italian Association of Medical Physics) formed a working group to define an Italian protocol for DBT. To date, the image quality control represents the most deficient section of the digital breast to-

mosynthesis quality control protocols. In fact, all the related tests are not yet characterized by either action levels or typical values. The image quality is assessed in terms of homogeneity and visibility of details, in the planes parallel to the detector, and z-resolution.
This thesis work focuses on the evaluation of one aspect of the image quality: the z-resolution. In detail, measurements were acquired in 24 DBT systems currently in use in 20 hospital facilities, in Italy. All the 7 mammography models present, to date, in public hospitals in our country were included in the study. The analysis was performed on the clinical reconstructed images of 5 different commercial phantoms, characterized by small details (0.32 mm - 1.00 mm) suitable for resolution assessment along the z-axis. It is essential to emphasize that the purpose of this thesis is not to compare the performance of the different mammography models tested. The goal is to propose a possible z-resolution QC test procedure and to identify characteristic values, for each type of DBT system involved in the study, that could be used as a starting point for defining typical values of z-resolution to be included, as a reference, in a DBT protocol.
This thesis is organized as follows: a theoretical introduction to radiation used in mammography and X-ray imaging of the breast is given, going into the details of DBT. A brief description of quality controls, characteristic of breast tomosynthesis, is also presented. Consequently, the 5 commercial phantoms and 24 DBT systems used, as well as the experimental setup and approach are described. Thus, the analysis of the empirical results follows a logical and chronological flow that first includes the preliminary study for defining the regions of interest on each phantom and for each DBT system, followed by the empirical evaluation of the repeatability of the measurements. Then, a physical interpretation of the obtained experimental results and a presentation of possible limitations of this work are supplied. Finally, conclusions are drawn in light of the results obtained.

Chapter 1

Radiation in mammography

1.1 Indirectly ionizing radiation

The term *radiation* can indicate both atomic or subatomic particles (e.g. electrons, neutrons, α or β particles) and electromagnetic waves (photons). In general, it defines a peculiar propagation of energy in space that does not involve the transport of macroscopic quantities of matter. It is possible to distinguish between ionizing (IR) and non-ionizing (NIR) radiation depending on the ability of the beam to cause ionization of atoms and molecules in the crossed medium. The latter in the medical field is typically human tissue. The discriminant factor for the IR/NIR classification is the value of the transported energy. Usually an energy value of 10 eV is sufficiently high to ionize matter and therefore to cause biological damages. Ionizing radiation, depending on the electrical properties, can be further classified into directly IR, i.e. charged particles that ionize atoms interacting through the Coulomb force, and *indirectly* IR. The latter is the typical case of photons and in general of neutral particles that do not interact strongly with matter. This means that the related ionization effects are due to secondary processes. Mammograms are performed using X-ray: ionizing beams of photons with typical energies of tens of keV, produced by changes in the kinetic of electrons. Two important characteristics of photons, exploited by radiology to obtain medical images, are the rectilinear trajectory and the ability to cross a medium. The thickness of matter that can be crossed depends on its composition and on the energy of the radiation: in general X-rays penetrate deeply through thick layers of matter.

1.2 X-ray interaction with matter

The knowledge of X-ray interaction with matter is essential for a correct choice of exposure conditions to be used in any particular clinical situation. At the energies of interest in mammography, photons interact with tissues through two main mechanisms: the *photoelectric effect* and the *Compton scattering*. The interactions are stochastic and their probabilities are defined in terms of cross-sections σ, conventionally expressed in units of area called barns. In this context σ can be thought as the effective area of a target atom that a photon must hit in order to interact. Each type of interaction has its own cross-section. It is useful to use different symbols to represent them: σ_{pe} will indicate the cross-section of a photon interacting with an atom through the photoelectric effect while σ_c will be used for the Compton scattering. The total cross-section σ_{tot} can be expressed as the sum of all the possible processes $\sum_i \sigma_i$. In this case $\sigma_{tot} \sim \sigma_{pe} + \sigma_c + ...$

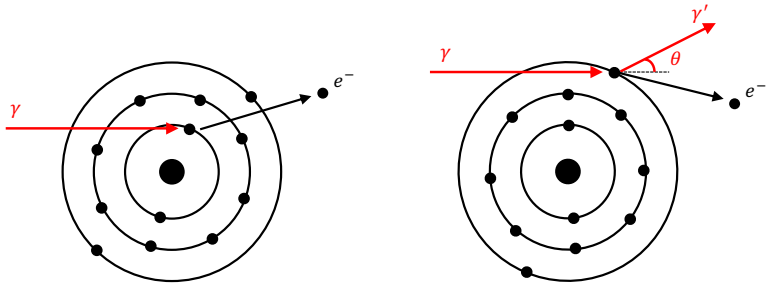

(a) *Photoelectric effect* (b) *Compton scattering*

Figure 1.1: Schematic representations of the two main interaction mechanisms between photons and matter at the typical energies of mammography.

1.2.1 Photoelectric effect

The photoelectric effect, schematically represented in Fig. 1.1a, consists in the complete release of energy by an incoming photon to an electron located in an atomic shell. The atom releases the excess energy by ejecting the electron, called *photoelectron*, with kinetic energy T:

$$T = h\nu - E_b, \tag{1.1}$$

where E_b is the electron binding energy of the atomic shell and $h\nu$ is the incoming photon energy. In more detail h is the Planck's constant while ν is the photon frequency. The ejected photoelectron is almost immediately stopped in the surrounding medium, since charged particles have a weak penetration power, but it leaves a vacancy in the atom which thus becomes a positive ion. The vacancy will be filled by an electron bounded in an higher atomic shell, with the resulting energy difference being carried off either by a *characteristic X-ray* or, with a different probability, by another electron known as Auger electron. The electron cascade will continue, resulting in the production of other characteristic radiation of lower energy, until the total emitted energy equals E_b. The characteristic X-rays are also called secondary radiation since they do not have any diagnostic importance and appear at low intensity. If they reach the detector, they contribute to the formation of noise, thus being detrimental for the image quality.
From the Eq. 1.1 it is possible to infer that the photoelectric effect can only take place if the photon energy exceeds the binding energy of the electron. Therefore X-rays, in agreement with their typical energies, can extract electrons up to the innermost shells. In fact, the most probable electron shell to lose an electron is the one that satisfies the energetic constraint and also that has the highest E_b. The photoelectric effect cross-section per atom, in the diagnostic photon energy range, is approximately:

$$\sigma_{pe} \sim \frac{Z^4}{(h\nu)^3}. \tag{1.2}$$

The expression indicates a very strong dependence on the material atomic number Z, as well as a strong inverse dependence on photon energy. The trend of σ_{pe} in function of $h\nu$ is characterized by sharp discontinuities, called absorption edges, that occur in correspondence of values just beyond the binding energy of atomic shells. The reason is that when $h\nu$ increases above the binding energy of a shell, all the orbiting electrons in that particular shell become available to be involved in the interaction. The most famous and evident absorption peak is called *K edge* which is referred to the closest shell to the nucleus, in agreement with the X-ray spectroscopic notation. The E_b of K shells, depending on the atomic number, are specific for each element: as Z of an element increases, so does its corresponding E_b and therefore the photon energy at which the K edge occurs must be higher. For this reason the most abundant elements in human tissue, e.g. hydrogen, carbon, oxygen, nitrogen, have K edges that are too low to be detectable ≤ 1 keV.

The photoelectric effect has both good and bad aspects in the field of the diagnostic radiology. The positive aspects are linked to the image quality: this kind of interaction does not produce a relevant diffused radiation, since it is very unlikely that the characteristic X-rays are able to reach the detector. This allows to improve the visibility of the different tissues which is greater when the difference in absorption between adjacent regions is large. Since $\sigma_{pe} \sim Z^4$, a good discrimination is expected for tissues that differ in the atomic number, such as soft and bone tissues. The negative aspect of the photoelectric effect is related to the patient exposure: the human body absorbs all the energy released by the incident interacting photons with the crossed tissues. This kind of interaction, among all the possible ones, is the main cause of dose for the patient. For this reason, radiological examinations are usually performed with relatively high energies to minimize the beam absorption. It is in fact necessary to find a good compromise between image quality and patient exposure.

1.2.2 Compton scattering

The Compton scattering is the interaction between a photon and a free electron. It is classified as a scattering process because the photon, releasing a portion of its energy to the electron, is deflected with a reduced frequency. The Compton effect can also occur in a medium, such as human tissue, where usually the outermost orbiting electrons are involved. This kind of interaction is schematically represented in Fig. 1.1b, where it is possible to observe the deflected photon and the recoil electron, called *Compton electron*. In agreement with the energy conservation law:

$$h\nu(\gamma^{'}) = h\nu(\gamma) - E_b - \frac{1}{2}m_e v^2, \tag{1.3}$$

where $h\nu(\gamma^{'})$, $h\nu(\gamma)$ are respectively the energies of the deflected photon and the incoming one, while $\frac{1}{2}m_e v^2$ is the kinetic energy of the recoil electron. The physical relationship between the photon energy, frequency and wavelength is: $E = h\nu = hc/\lambda$. It is therefore possible to describe the variation of the photon energy in function of the scattering angle θ, using the concept of wavelength:

$$\Delta\lambda = \lambda^{'} - \lambda = \frac{h}{m_e c}(1 - \cos\theta), \tag{1.4}$$

where λ', λ are respectively the wavelengths of the diffused photon and the incoming one, while c is the speed of light. According to the equation the photon can be deflected in any direction including the backward one for $\theta = 180°$ but, as the incoming photon energy grows, the angular distribution of the scattered photons is increasingly narrow in the forward direction, θ=0°. This fact constitutes a serious problem in diagnostic radiology, where the used energy values cause the scattering at small angles of a non negligible portion of X-rays. This means that some photons lose little of their initial energies and that the energies imparted to the recoil electrons are negligible. In this way also the scattered photons are able to reach the detector, thus contributing to the background noise. Still nowadays there is no way to recognize the diffused radiation at small angles therefore it is always necessary to take into account this detrimental contribution.
In radiology, another negative aspect of this type of interaction is related to the fact that the material invested by the primary X-ray beam becomes a secondary source of radiation. This means that the personnel conducting the examination, in particular in interventional radiology, is exposed to the radiation scattered from the close patient body. This is not the case of mammography as the radiologic technologist can remain behind leaded glass during the whole examination.
So far the kinematics of the interaction was described. Regarding the probability of the interaction, the Klein-Nishina formula provides the differential cross-section $d\sigma_e/d\Omega$ (i.e. the probability that a photon will be scattered in the solid angle element $d\Omega$) for the free electron case:

$$\frac{d\sigma_e}{d\Omega} = \frac{r_e^2}{2}(1 + \cos\theta^2) f_{KN}, \tag{1.5}$$

where $r_e \sim 2.82$ fm is the classical radius of the electron and

$$f_{KN} = \left[\frac{1}{1 + \alpha(1 - \cos\theta)}\right]^2 \left[1 + \frac{\alpha^2(1 - \cos\theta)^2}{(1 + \cos\theta^2)[1 + \alpha(1 - \cos\theta)]}\right]. \tag{1.6}$$

The parameter α is defined as $h\nu/m_e c^2$. The total Compton cross-section σ_e is obtained by integrating the Eq. 1.5 over the whole solid angle Ω, using for θ the angular range [0°, 180°]. For incoherent scattering with atoms, the contributions from individual electrons are added and the differential cross-section takes the form:

$$\frac{d\sigma_c}{d\Omega} = \frac{r_e^2}{2}(1 + \cos\theta^2) f_{KN} S(p, Z). \tag{1.7}$$

The function S, called incoherent scattering, is a universal function of the momentum transfer quantity p and the atomic number. The value for S is zero in the forward direction and increases with increasing p, reaching the value of Z. This increase becomes slower as the atomic number is higher. The total cross-section σ_c in many situations, is almost equal to the single electron cross-section σ_e multiplied by the atomic number of the atom: $\sigma_c = Z\,\sigma_e$.
It must be noticed that when diagnostic energy photons interact with materials of low Z, e.g. soft tissue, the Compton process dominates the others.

1.3 X-ray attenuation and contrast formation

When a photon beam crosses a slab of a material there are two different possibilities: the photons can exit the slab unaltered, retaining their initial energy, or they can interact with the traversed medium. In the previous section, the two most important mechanisms of interaction, in mammography, between X-rays and matter have been explained. Both mechanisms of interaction contribute to reducing the number of photons in the beam that crosses the slab: the photoelectric effect involves the absorption of the photons, which are thus subtracted from the beam, while the Compton effect causes the deflection of photons from their incident direction. The total attenuation of a monochromatic beam is obtained from the *Beer-Lambert law*, which describes an exponential attenuation with the crossed thickness x:

$$I(x) = I_0 e^{-\mu x}. \tag{1.8}$$

In the previous expression I_0, $I(x)$ are respectively the incoming and outgoing X-ray beam intensities. The parameter μ, called *attenuation coefficient*, represents the fraction of photons removed from the monochromatic beam per unit thickness of crossed material. It is defined as:

$$\mu = N\sigma_{tot} = \left(\frac{N_A \rho}{A}\right)\sigma_{tot}, \tag{1.9}$$

where N_A is the Avogadro's number, ρ and A are respectively the density and the mass number of the material. When a medium formed by a complex set of elements is considered, the weighted average of the atomic numbers of all the elements involved must be used. The attenuation coefficient, being a function of the total cross-section (1.9), depends on the energy of the photons

and on the atomic number of the crossed medium.
Exploiting the Beer-Lambert law it is possible to define an interesting property of an X-ray beam called Half Value Layer (HVL). The HVL is defined as the thickness of a specific material required to reduce the intensity of a photon beam to one half of its initial value:

$$HVL = \frac{1}{\mu} \ln\left(\frac{I_0}{I}\right) = \frac{\ln(2)}{\mu}. \tag{1.10}$$

It is inversely related to the linear attenuation coefficient.
The determination of the HVL in radiology is a way of characterizing the penetrability of an X-ray beam. In fact, when evaluated under good geometry conditions, the HVL is an indirect measure of the effective energy (also referred to as the quality) of a beam. In diagnostic radiology, aluminum is commonly chosen as the medium, giving the HVL in unit of mm Al.
A fundamental application of the Beer-Lambert law in radiology is the creation of medical images with variable contrast, as a consequence of the different X-ray absorption in tissues. The contrast is defined as the difference in the grey levels between closely adjacent regions in the image. Different types of contrast are defined in the imaging process, i.e. detector contrast, displayed contrast, etc. The one linked to 1.8 is the *subject contrast* C_s, defined as the contrast of the imaged object. This strictly depends on the X-ray spectrum and on the attenuation of the object itself. For example, in Fig. 1.2 it is schematically represented the transmission of an X-ray beam with intensity I_0 at two different thicknesses of the same material that differ by a thickness z. The subject contrast is thus defined as: $C_s = (I_A - I_B)/I_A = 1 - e^{-\mu z}$, where $I_A = I_0 e^{-\mu x}$ and $I_B = I_0 e^{-\mu(x+z)}$ are the transmitted intensities. This means that C_s increases exponentially with either μ or z. The other types of contrast are more related to the performance of the devices, such as detectors or displays, rather than to physical phenomena strictly related to radiation.

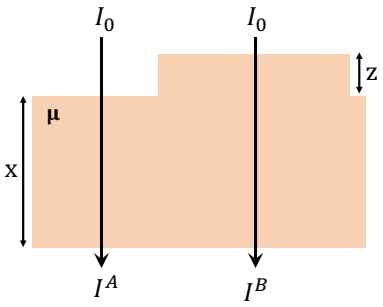

Figure 1.2: Subject contrast.

In Fig. 1.3, the overall X-ray image formation process in radiology is schematically represented. It is possible to observe that the X-ray beam is attenuated

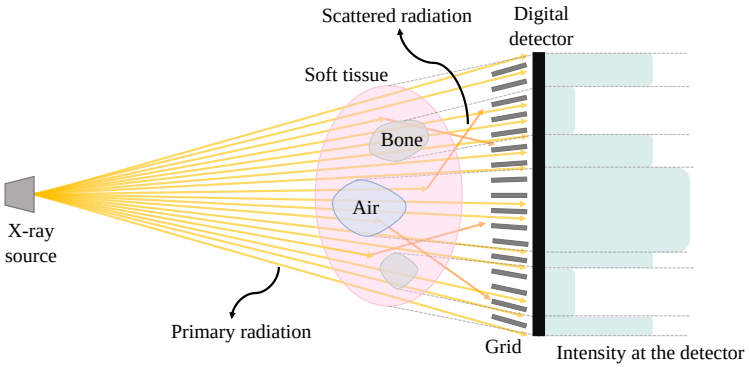

Figure 1.3: Schematic representation of the X-ray image formation.

differently according to the crossed tissues and that a portion of the beam interacts, thus being scattered at different angles and consequently lost.

1.4 Dosimetric quantities

Radiation dosimetry in the fields of health physics and radiation protection is the measurement, calculation and assessment of the ionizing radiation dose absorbed by an object, usually the human body. This applies both internally, due to ingested or inhaled radioactive substances, or externally due to irradiation by external sources, such as in the case of X-ray. The energy released by radiation in the crossed tissues is responsible for different effects that can have an harmful biological impact, e.g. a rise in temperature or chemical and physical changes in the material properties. For this reason, different dosimetric quantities have been defined to directly measure or to estimate radiation detriment or risk.

1.4.1 Kerma

The kerma K is related to the energy transferred from indirectly ionizing radiation (i.e. uncharged particles such as photons and neutrons) to matter. Kerma is the acronym for Kinetic Energy Released per unit Mass and it is defined as:

$$K = \frac{dE_{tr}}{dm}. \tag{1.11}$$

In the previous expression the quantity dE_{tr} is the expectation value of the energy transferred from indirectly ionizing radiation to charged particles in the elemental volume dV of mass dm. The SI unit of K is joules per kilogram (J/kg), which is given the special name gray (Gy).
Since K may be defined in any material, including air, it is always important to declare the chosen medium.

1.4.2 Absorbed dose

The absorbed dose D is defined simply as the energy E_{abs} imparted by ionizing radiation to an elemental volume dV with mass dm:

$$D = \frac{dE_{abs}}{dm}. \tag{1.12}$$

Absorbed dose is expressed in the same units as kerma, i.e. gray (Gy). The two quantities (D and K) are in fact connected, but not equal. The absorbed dose is defined as the total amount of energy deposited by ionizing radiation in a substance whereas kerma is defined as the sum of the initial kinetic energies of all the charged particles, liberated by uncharged ionizing radiation in a substance. At low energies, K approximately equals D, since most of initial kinetic energies of all the charged particles deposit their energy in the sample. At higher energies K is larger than D, because some highly energetic β particles and X-rays escape the region of interest before depositing their energy. The escaping energy is counted in K, but not in D.

1.4.3 Equivalent dose

Different types of ionizing radiation can cause biological effects of different magnitudes for the same value of the absorbed dose. This means that it is convenient to define a quantity specifically related to a particular type of radiation. The equivalent dose H_T, for a certain radiation R, is defined as:

$$H_T = w_R \, D_{T,R}. \tag{1.13}$$

In this expression $D_{T,R}$ is the absorbed dose averaged over a tissue or an organ T (due to radiation R), while w_R is the radiation weighting factor. It represents the relative biological effectiveness of the incident radiation in producing effects in T. In accordance with the ICRP 103 Recommendations [1], photons have w_R=1. The SI unit for equivalent dose is the sievert (Sv).

Organ/Tissue	w_T
Lung, stomach, colon, bone marrow, breast, reminder	0.12
Gonads	0.08
Thyroid, oesophagus, bladder, liver	0.04
Bone surface, skin, brain, salivary gland	0.01

Table 1.1: Tissue weighting factors, ICRP 103 [1].

1.4.4 Effective dose

Different tissues and organs of the human body have a different response to radiation. One part of the body may be more or less radiosensitive than its neighboring regions. For this reason, a quantity has been defined, called effective dose E, which takes into account the type of radiation and also the body region exposed. In the ICRP 103 Recommendations, fifteen different parts have been identified in the human body, each characterized by its own tissue weighting factor w_T. The values are reported in Tab. 1.1. It can be deduced that the breast, being characterized by the highest w_T, is very radiosensitive. The sum over all the organs and tissues of the body of w_T is unity. The formal definition of the effective dose is:

$$E = \sum_T w_T \, H_T. \tag{1.14}$$

It is the sum over each irradiated body part of the product of equivalent dose and of the appropriate tissue weighting factor, which represents the contribution of that organ or tissue to the total detriment resulting from uniform irradiation of the whole body. The effective dose is expressed in the same units as equivalent dose, i.e. sievert (Sv).

1.5 Principles of radiation protection

Radiation protection is the discipline applied to the protection of humans and the environment from the harmful effects caused by ionizing radiation. The International Commission on Radiological Protection (ICRP) is an organization with the mission to develop a system of radiation protection that allows the many beneficial uses of radiation to be realized, while ensuring detrimental radiation effects are either prevented or minimized. The fundamental assumption on which the ICRP is based is that there is no dose,

however small, to which a certain risk can not be associated. For this reason three fundamental principles, that must be fully implemented in the legislation of each country, have been defined.
1. *The principle of justification*: any decision that alters the radiation exposure situation should do more benefit than harm. In other words, the introduction of a radiation source should result in sufficient individual or societal benefit to offset the detriment it causes.
2. *The principle of optimisation*: the likelihood of incurring exposures, the number of people exposed and the magnitude of their individual exposure should all be kept, taking into account economic and societal factors, as low as reasonably achievable (ALARA principle).
3. *The principle of dose limitation*: the dose to individuals from planned exposure situations, other than medical exposure of patients, should not exceed the appropriate limits recommended by the Commission.
The ICRP recognises three categories of exposed individuals: workers, patients and members of the public. These categories are respectively known as occupational, medical and public exposure. Occupational exposure is generally interpreted as radiation exposure of individuals as a result of their work. However, as radiation is ubiquitous, only those exposures that can reasonably be regarded as the responsibility of the operating management are included. Medical exposure is predominantly that of patients but also includes exposures incurred by those caring for patients, other than as part of their occupation, and exposures incurred by volunteers as part of biomedical research programs, where there is no direct benefit to the volunteer. Public exposure then incorporates all exposures other than medical and occupational. In radiology practices unauthorized access by the public to functioning X-ray rooms must be prohibited, so the public exposure should not be particularly relevant. The only important aspect is the dose assessment in the areas surrounding radiology facilities that are accessible to the public. Dose constraints may be applied, where appropriate, in the design phase of the building and of X-ray rooms.

1.5.1 Occupational exposure in radiology practices

In the X-ray department, workers who are normally exposed to radiation are medical doctors, medical physicists, radiologic technologists and nurses. It is the joint responsibility of the employer and licensee to ensure that occupational exposures are limited and optimized and that suitable and adequate

facilities, equipment and services for protection are provided. For a monitoring program, individual dosimeters must be worn by workers to estimate either the effective dose or an equivalent dose to an organ, e.g. the fingers.

Figure 1.4: My personal "whole-body" dosimeter.

There are in fact many types of individual dosimeter, the most used is the "whole-body" dosimeter, represented in the above figure. It must be worn on the chest, on the outside of clothing. This location monitors exposure of most vital organs and represents the bulk of body mass, thus representing the dose to the whole body. In all cases, whether whole body or extremity dosimeter is to be used, the monitoring period should ideally be one month, and should not exceed three months. Results of the monitoring program should be shared with staff and used as the basis for implementing and reviewing dose reduction strategies. The following three basic physical principles can be implemented to reduce occupational exposure:
1. Restrict the time for which a person is exposed to radiation as much as possible. The longer the exposure, the greater the cumulative dose.
2. Ensure that the distance between a person and the X-ray source is kept as large as practicable. Radiation from a point source follows the *inverse square law*, i.e. double the distance means a quarter of the dose. For larger sources, such as scatter from a patient, the inverse square law will not be accurate over short distances and a smaller power than two will be needed. However, as an approximation, and at distances normally used for protection purposes, the inverse square law can still be used.
3. Employ appropriate measures to ensure that the person is shielded from the source of radiation. Materials of high atomic number and density such as lead or steel are commonly used for facility shielding.
The ICRP recommended occupational dose limit for planned exposure situations, such as the use of X-ray in radiology, is an effective dose of 20 mSv per

year, averaged over defined periods of 5 years. With the further provision that the effective dose should not exceed 50 mSv in any single year.
In our country, important innovations in the field of prevention and protection from ionizing radiation have been introduced in the recent Legislative Decree no. 101 [2] of 31 July 2020, which entered into force on 27 August 2020. The provision, which adapts national legislation to the oldest European Directive 2013/59/Euratom, repeals and replaces, in particular, Legislative Decree no. 230/1995. According to the new Decree, an individual can be classified as *exposed worker* if, in relation to his work activity, he has a likelihood to receive doses exceeding the following limits in a (calendar) year:

- an effective dose of 1 mSv,
- an equivalent dose of 15 mSv to the lenses of the eye,
- an equivalent dose of 50 mSv to skin or extremities.

Exposed workers can be classified in two categories for monitoring and surveillance purposes: Category A and Category B workers. The latter are exposed workers who have a likelihood to receive in a calendar year:

- an effective dose of 6 mSv,
- an equivalent dose of 15 mSv to the lenses of the eye,
- an equivalent dose of 150 mSv to skin or extremities.

In category A exposed workers have a likelihood to receive, in a calendar year, doses exceeding the ones of category B.
During a mammography examination relatively low doses are used and the radiologic technologist can stay away from the X-ray beam. This means that the occupational exposure involved is not particularly high and is further reduced thanks to the use of a protective leaded glass, behind which the professional stands during the whole examination.

1.5.2 Medical exposure in radiology practices

Dose limits are not defined for patients undergoing medical exposures. The reason of the different treatment afforded to medical and occupational/public exposures is that, in the first case there is both a benefit and a detriment whereas for the others there is only a detriment. Despite this exception, the philosophical basis for the management of medical exposures in diagnostic radiology is based on the avoidance of unnecessary doses, through the application of the principles of justification and optimization. For this reason, a medical physicist must calibrate all the used sources and perform an assessment of the typical doses for all the procedures performed in the facility.

A very important tool in the optimization process is the use of Diagnostic Reference Levels (DRLs). DRLs are dose levels for typical examinations of groups of standard-sized patients and for broadly defined types of examinations. They do not represent a constraint on individual patient doses but give an idea of where the boundary between normal practice and abnormal practice lies. Periodic assessments of typical patient doses (or the appropriate surrogate) for common procedures are performed in the radiological facility and comparisons are made with DRLs.
During mammography examinations the lowest possible doses are used, compatibly with a diagnostic acceptable image quality. For this reason mammograms belong to dose class I, i.e. less than an effective dose of 1 mSv. This dose classification, which includes four classes in order of increasing dose (from I to IV), is very recent and it is only used in our country. In fact, among the key innovations in the medical field of the D.Lgs. 101/2020 there is the inclusion of information relating to exposure in the final report of all radiological examinations, as required by the provisions of Directive 2013/59/Euratom. To date, there is no a European dosage class communicable to the patient, therefore Italy has temporarily identified the four classes.

1.5.3 Special practices

An interesting innovation introduced in the Legislative Decree no. 101 is the identification of *special practices*. These includes the exposure of patients:

a) in pediatric age,
b) in screening programs (e.g. mammography examinations),
c) in high dose radiology practices (e.g. interventional radiology, CT),
d) in radiotherapy treatments.

The peculiarity of special practices is that they expose the patient to a relatively high radiological risk. In detail in the case of screening programs, such as mammography examinations, the risk is linked to the fact that a large group of asymptomatic patients are periodically exposed. The Decree states that all these procedures must be performed in compliance with the principles of justification and optimization. Moreover, training activities are provided for health professionals involved in the practices. In cases a) and b), the person in charge of the radiological system ensures that the medical physicist performs periodic dosimetric evaluations for all the situations in which no DRLs are available. For mammography screening the diagnostic reference levels are defined in the ISTISAN report 20/22 [3].

Chapter 2

Breast X-ray imaging

2.1 Breast cancer issue

Breast cancer is one of the leading causes of cancer death in women: it is estimated to account for nearly one third of all cancers affecting them. The disease has a wide geographic variability, with rates up to ten times higher in the most economically developed countries. The main risk factors are age, hormonal factors, dietary and metabolic factors, previous breast neoplasms, family history and heredity. Early diagnosis plays an essential role in reducing mortality rates and in improving patient prognosis. For this reason mammographic screening programs have been started in several countries. In Italy the screening is addressed to women between the ages of 50 and 69 and it is performed with a mammogram every two years (it is to be noticed that some regions have not joined yet). In some regions, such as Emilia-Romagna, screening is being tested between the ages of 45 and 74. In the event of a suspicion, the first examination is followed by further investigation.
According to AIOM [4], about 55.000 new diagnosis have been estimated in 2020 in our country (estimates for 2021 are not available yet). The incidence of breast cancer is geographically uneven: statistics confirm a higher incidence in the Italian northern regions (163 cases for 100.000 inhabitants), compared to the Center (145 cases for 100.000 inhabitants) and South-Islands (124 cases for 100.000 inhabitants) [5].
Since the late 1990s there has been a moderate but constant trend of decreasing mortality from breast cancer (-1.4%/year), attributable to greater diffusion of screening programs and to therapeutic progress [6].

2.2 Breast anatomy

The female breast is a glandular organ located in the front of the rib cage, extending from the second rib above to the sixth rib below. Medially, it borders the lateral edge of the body of the sternum, and laterally it reaches the mid-axillary line. The breast serves as the mammary gland, which produces and secretes milk to feed infants. It is predominantly composed by adipose tissue and glandular tissue, characterized by variable proportions that vary according to several factors [7]. For example, in breastfeeding women the glandular tissue is more abundant. Furthermore, the percentage of glandularity is predominant in youth, but tends to decrease with increasing age. The proportionality between fat and glands determines the density or firmness of the breast. Dense breasts are related to a higher risk of developing cancer. During a woman's life, the breast changes size, weight and composition due to hormonal changes, menstrual cycle, pregnancy, breastfeeding and to menopause. Morphologically the breast is tear-shaped. The superficial tissue layer is separated from the skin by few centimeters of adipose tissue. The breast contains about fifteen lactiferous lobes that converge at the nipple. The milk ducts are immediately surrounded with dense connective tissue that support the glands. Milk exits the breast through the nipple, which is surrounded by a pigmented area of skin called the areola. The fat fills in the spaces between glands and connective tissue and largely determines the breast size. Breast size and weight vary widely among women. A small/medium sized breast weighs 500 grams or less, while a large one can weigh up to one kilogram or more. Most breast cancers are *adenocarcinoma*: they involve the mammary gland cells of the milk ducts or lobules. The radiologist that analyzes a mammogram will look for different types of breast anomalies such as small white spots called *calcifications* and abnormal areas called *masses* or *spiculations*. A calcification is a tiny calcium deposits within the breast tissue and may be caused by cancer. It looks like a small white spots on a mammogram and, depending on its size, can be classified as macro or micro. A mass is an area

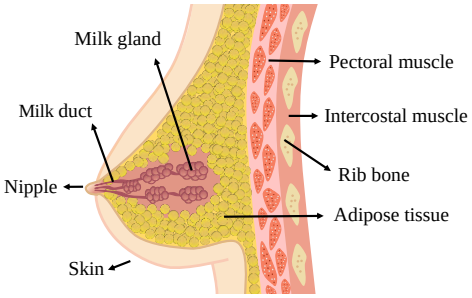

Figure 2.1: Illustration of the female breast.

of abnormal breast tissue with shape and edges that make it looks different than the rest of the breast tissue. Masses can be many things, including cysts, but they may also be a sign of cancer. Spiculation is a stellate distortion caused by the invasion of breast cancer into adjacent tissue. Unless it appears in the site of a previous biopsy or a surgical treatment, a spiculated margin is highly suspicious of malignancy.

2.3 Digital mammography

Mammography is an optimized examination for the breast. It represents one of the most demanding radiographic applications, simultaneously requiring excellent contrast sensitivity, high spatial resolution and wide dynamic range, at the lowest breast radiation dose that is reasonably achievable by meeting the other requirements. Currently, mammography is the gold standard among modalities applicable to the screening and diagnosis of breast cancer. In fact, it is used both to diagnose symptomatic or suspicious patients and to perform screening programs on large groups of asymptomatic women in selected age range. A typical mammographic screening examination consists of one or two views of each breast. Common projections, represented in the following figure, include the Cranial–Caudal (CC) and Medio-Lateral Oblique (MLO). A diagnostic examination can include other projections and possibly even enlargements of the suspicious area.

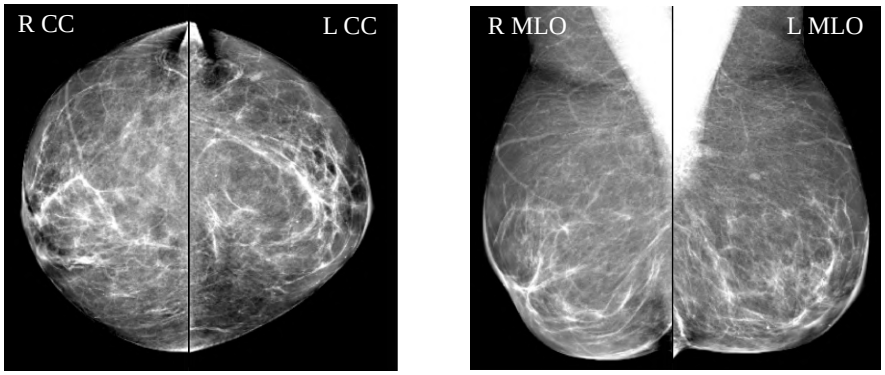

Figure 2.2: Cranial-caudal and medio-lateral oblique projections. Images courtesy of the Santa Maria delle Croci hospital, Ravenna.

Digital mammography, also called *Full-Field Digital Mammography* (FFDM), was introduced commercially in 2000. As suggested by the name this type of mammography is characterized by a solid-state detector or by a scintillator, coupled with a photodetector, that converts the transmitted X-rays from the breast into electrical signals. Its predecessors are the screen film mammography and the Computed Radiography (CR) system. The first is based on the use of a high resolution fluorescent screen and a coupled film that absorb the transmitted X-rays and convert them into an optical image. The second represents a transition phase between analog and digital approach: it uses a photostimulable phosphor-based casset that must be properly read by a special mammo CR reader and then digitized into a computer.

Figure 2.3: Mammography system: *Hologic Selenia Dimensions*.

To date, the full digital approach has achieved acceptable spatial resolution performance from a diagnostic point of view. Furthermore, clinical studies have shown that FFDM and screen film mammography detect and miss comparable numbers of biopsy-confirmed breast cancers. The main advantage of a FFDM is that image acquisition, processing, display and storage are performed independently, allowing the optimization of each. As the image is stored digitally, it can be displayed on a computer screen with the ability to apply post-processing operations to facilitate the radiologist's diagnosis. This means that examination retakes, common with X-ray films, are virtually no more needed with the digital approach. In fact also non-optimally exposure conditions can give a good diagnostic image, after the application of image processing tools.
In Fig. 2.3 is shown the Hologic Selenia Dimensions, an example of a digital mammography system. It is currently in use in Ravenna at the "Santa Maria delle Croci" Hospital and it allows to perform the examination both in FFDM - 2D modality and in tomosynthesis modality.

2.4 Digital breast tomosynthesis

Digital breast tomosynthesis (DBT) is an advanced form of mammography. It relies upon the reconstruction of a pseudo-volumetric image from the acquisition of multiple projections over a limited angular range. Imaging three-dimensional anatomy via a planar image has obvious defects because overlapping tissues degrade cancer detection quality by decreasing sensitivity and specificity. In DBT, the X-ray source moves in an arc over the breast capturing multiple images from different angles, as illustrated in Fig. 2.4. According to the DBT system, the X-ray source can move in a continuous way or act in a step-and-shoot mode, which means that the source stops for each image to be acquired. The step-and-shoot mode reduces the blurring caused by the movement of the X-ray source but increases the duration of the examination compared to the continuous mode. Currently, the tomosynthesis systems have acquisition ranges that vary from 15° to 50° (considering the entire rotation 2θ) and typically acquire 9-25 projection images. The specifications for the most recent systems are reported in Tab. 2.1.

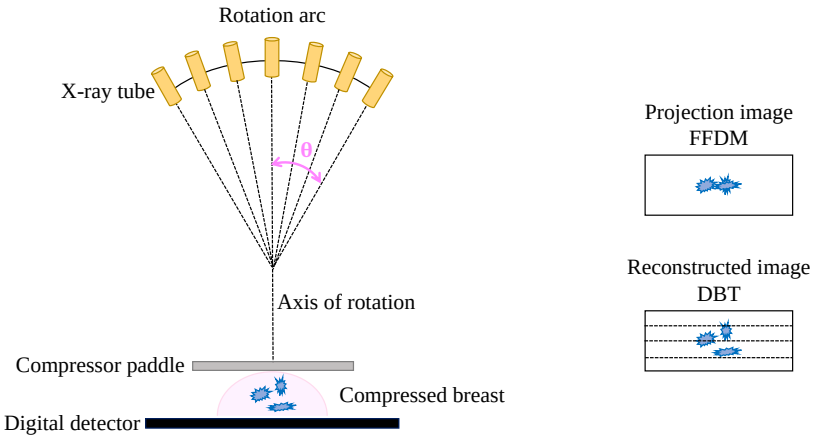

Figure 2.4: Scheme of a generic system for tomosynthesis. The theoretical images, respectively obtained by FFDM and by DBT, are shown alongside.

Due to the limited acquisition angle, tomosynthesis is characterized by an anisotropic resolution: the planes parallel to the detector have an higher resolution than the X-ray direction of propagation. However, the latter (z-axis) has a high enough resolution to reduce the problems related to the

Mammography system	Motion	Angular range	Projections
GE Healthcare SenoClaire	Step&shoot	25°	9
GE Healthcare Pristina	Step&shoot	25°	9
Hologic Selenia Dimensions	Continuous	15°	15
Hologic 3Dimensions	Continuous	15°	15
IMS Giotto Class	Step&shoot	30°	11
Siemens Mammomat Inspiration	Continuous	50°	25
Siemens Mammomat Revelation	Continuous	50°	25
Fujifilm Amulet Innovality	Continuous	15°- 40°⋆	15

Table 2.1: Source motion, angular range and number of acquired projection images in the most recent DBT systems in the market.
⋆ It is possible to choose an angular range of 15° for the standard (ST) mode and of 40° for the high resolution (HR) mode.

overlapping of tissues. The acquired projection views are reconstructed to provide sections parallel to the detector at different heights z_i as reported in Fig. 2.4, where the image obtained with a DBT system is schematically represented. In this way it is possible to minimize the tissues overlap typical of planar radiography, i.e. FFDM, that may hide the presence of tumors or make it difficult to distinguish the healthy tissues overlapped in the image from tumors. The reconstructed planar sections can be stacked together to generate a pseudo-volumetric image or can be combined to provide a virtual two-dimensional image, similar to a single projection, called *synthetic image*. The latter is not equivalent to digital mammography images, since it is reconstructed from the DBT dataset through specialized algorithms.
According to the Italian College of Breast Radiologists [8], evidence available for DBT allows to recommend its usage for all cases of symptomatic women and patients needing work-up of two-dimensional mammography suspicious findings. sFFDM/DBT protocols should be preferred to examine symptomatic women, if possible. The acronym sFFDM refers to the synthetic mammogram obtained from the DBT dataset. These protocols have solved the increase in radiation exposure associated with the FFDM/DBT approach, called "combo" modality, which consists in the separate acquisition of FFDM and DBT. Nowadays, for population-based screening, the main priority is to shift from analog film-screen mammography and computed radiography systems, that are still in use, to full-field digital mammography. In order to use

the DBT as a first-level screening tool, specific evidence is still needed. This is particularly relevant for a significant statistically and clinically reduction in interval cancer rate. When this evidence will be available, asymptomatic women with both intermediate and high risk (including those with a previous breast cancer history) will be allowed to be screened with DBT on a routine basis. However, high-risk women to whom a mammogram has been prescribed should already be examined with a sFFDM/DBT protocol.
To date, the most recent mammography systems are able to perform both FFDM mammograms, keeping the X-ray source fixed over the detector, and DBT ones, letting the source to move in an arc.

2.5 Mammography equipment

The basic components of a mammography system of any type, in particular the two most recent ones - FFDM and DBT, are always the same. The key elements are the X-ray tube, the compressor, the breast support in which are placed the anti-scatter grid and the detector, and the Automatic Exposure Control. All these components are described below.

2.5.1 X-ray tube

The differential absorption of X-rays in tissues and organs, owing to their atomic composition, is the basis for the various imaging methods used in diagnostic radiology. X-rays are produced through *X-ray tubes*, capable of converting electrical input power into radiation. Typically they consist of a vacuum envelope inside which there are a cathode and an anode. The cathode is negatively charged and consists of a filament that, heated at incandescence by a low-voltage electric current, emits electrons by thermionic effect. The anode, being positively charged, is the target and its material influences the produced X-ray spectrum. In radiology the materials usually used for the anode are characterized by an high atomic number, an high melting point and an high heat dissipation capacity. A high potential, expressed as kilovolts (kV), is applied between the cathode and the anode to accelerate the electrons towards the target. Their collision against the anode produces a significant loss of kinetic energy. Most of the electron energy, typically about the 99%, is converted into heat and must be effectively dissipated. The remaining 1% is used to produce X-rays, that are generated

in two possible different ways: *bremsstrahlung radiation* and *characteristic X-rays*. When fast electrons slow down by Coulombic interaction with the electrostatic field of a target nucleus, they emit X-ray photons also known as bremsstrahlung radiation. The amount of energy irradiated depends on the closeness of the approach between the fast electron and the target nucleus. This means that bremsstrahlung radiation can have a range of energies from zero, for an ideal infinite distance, up to a maximum value equal to the kinetic energy of the electron, for a front impact. The energy spectrum of bremsstrahlung radiation is therefore of continuous type. The other way in which X-rays are produced is very similar to the photoelectric effect. The main difference is in the colliding particle which is an electron in this case. In fact, fast colliding electrons remove orbiting electrons from the innermost shells of a target atom. When this happens, the electrons belonging to higher shells jump into the created vacancies and, in this process of rearrangement, X-ray photons are emitted with energies equal to the difference between the binding energies of the two shells. The emitted photons are therefore called characteristic X-rays and the related energy spectrum is a line spectrum, with peaks that occur in different positions depending on the material of the anode. Since both bremsstrahlung and characteristic X-rays are produced simultaneously, the resulting X-ray spectrum is the overlap between the continuous and the line spectra. The produced X-rays must exit the tube to be used in practice and usually the exit window is made of beryllium, a light element. It allows to minimize the absorption of the X-ray beam as it passes through the window of the tube, which is particularly important when using low-energy X-rays such as in mammography, because of their preferential absorption. When the X-ray beam exit the tube the overall intensity is not spatially homogeneous, in fact the field intensity towards the cathode is more than that towards the anode. This is due to the so called

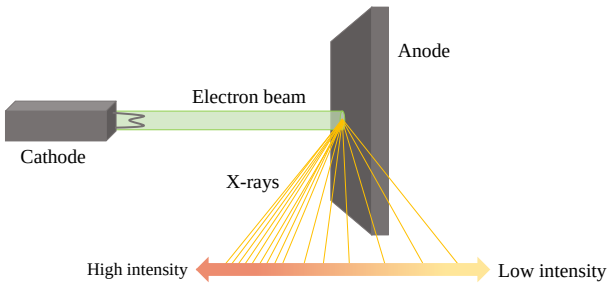

Figure 2.5: Schematic representation of the heel effect.

Heel effect, schematically represented in Fig. 2.5, which refers to the lower field intensity towards the anode with respect to the cathode, due to a lower probability of X-ray emissions from the target at angles perpendicular to the electron beam. The conversion of the electron beam into X-rays does not simply occur at the surface of the anode but deep within it, so they must traverse back out of the anode before they can proceed toward the exit window. At emission angles that are perpendicular to the electron beam must be traversed a greater material thickness with respect to those more parallel to it. This increase in thickness leads to more resorption of the radiation by the target itself, resulting in fewer X-rays emitted at angles perpendicular to the electron beam. This effect is not negligible in mammography and, to avoid artifacts in the final image, corrections must be applied to the detector. The output of the X-ray tube depends on the anode material, that affects the efficiency of bremsstrahlung photons and the quality of the characteristic X-rays and on the used tube voltage and current. The tube voltage, expressed as *peak kilovoltage* (kVp), determines the maximum energy of the spectrum and the efficiency of the X-ray production. At higher kVp both the overall intensity and the proportion of more energetic X-rays increase. Therefore, by controlling the kVp, the penetrative characteristics of the X-ray beam can be changed. Moreover, the exposure of the patient is related to the square of the kVp value. The tube current, expressed in milliampere (mA), is proportional to the number of electrons that travel from the cathode to the anode, per unit time. This means that as the current is increased, more X-rays are produced but the energy distribution in the spectrum remains the same. The practical effect of increasing current is to decrease the time required to radiograph an object. If the object is very dense and difficult to penetrate, increasing the current will not improve the results because the penetrating power of the beam is not increased. The tube current–exposure time product is sometimes referred to as the "tube loading" and is expressed in mAs, where the time factor corresponds also to the electrons production duration in the tube.

As in general radiography, in mammography the main object is to define a spectrum that provides energies that ensure a good compromise between radiation dose and image quality. The spectral shape is controlled by adjusting the previously described exposure parameters and the type and thickness of the metallic filter placed between the X-ray tube and the breast. Filters are used to provide selective removal of X-rays before they reach the patient. In particular it is necessary to absorb low-energy radiation, that would oth-

Mammography system	FFDM Target/Filter	DBT Target/Filter
GE Healthcare SenoClaire	Mo/Mo, Mo/Rh, Rh/Rh	Mo/Mo, Mo/Rh, Rh/Rh
GE Healthcare Pristina	Mo/Mo, Rh/Ag	Mo/Mo, Rh/Ag
Hologic Selenia Dimensions	W/Rh, W/Ag	W/Al
Hologic 3Dimensions	W/Rh, W/Ag	W/Al
IMS Giotto Class	W/Ag	W/Ag
Siemens Mammomat Inspiration	W/Rh*	W/Rh
Siemens Mammomat Revelation	W/Rh	W/Rh
Fujifilm Amulet Innovality	W/Rh	W/Al

Table 2.2: Anode and filter possible combinations, for FFDM and DBT modalities, in the most recent mammography systems in the market.
* It is available also the combination Mo/Mo for breasts thinner than 2 cm.

erwise be completely absorbed by the tissue thus increasing the dose but contributing little to image formation, and higher-energy radiation which would degrade the subject contrast being characterized by a high penetration power. In general, the choice of the filter coincides with the material of which the anode is made: in this way it is possible to exploit the effect of the K edge to absorb high-energy X-rays. Historically in mammography the most used anode material is molybdenum Mo, commonly employed with a Mo filter that is tens μm thick. This filter acts as an energy window, providing greater attenuation of X-rays both at low energies and above the K absorption edge at 20 keV. Although molybdenum spectra are relatively well suited for imaging a breast of average attenuation, slightly higher energies are desirable for imaging thick and dense breasts. The average energy of the beam can be increased by employing anode and/or filters of higher atomic number than molybdenum, such as rhodium Rh that has a K absorption edge at 23 keV. In this way it is obtained a spectrum with increased penetration, compared with the Mo/Mo combination. In modern mammography systems, it is possible to select the most suitable filter once the characteristics of the subject to be examined are known. Nowadays the use of a new anode material is widespread: tungsten W, which can be associated with different types of metallic filters. In Tab. 2.2 all the anode and filter material possible combinations used in the most recent mammography systems in the market, both for the FFDM and DBT modalities, are reported.

The major differences relating to the X-ray tube between the two modalities of mammography examination are found in the choice of the target/filter, as already mentioned, and in the acquisition time of a single projection. The latter corresponds to the time interval during which the tube must emit X-rays. In FFDM, single "high dose" projections are acquired and the tube, based on the mAs value, produces a single and long pulse in the order of seconds. According to RP 162 [9], to avoid artifacts related to patient movement, the acquisition time for a single projection should not exceed two seconds for a standard-thick breast. In DBT, the total acquisition time is greater since it is given by the sum of many "low dose" projections. In fact, to keep the irradiation comparable to the FFDM modality, since the patient in breast tomosynthesis is no longer exposed once, each single projection is acquired with lower mAs values in the order of milliseconds. The tube then emits short pulses of radiation as can be seen in Fig. 2.6, where the comparison between typical X-ray pulses respectively for an FFDM and DBT examination are shown. In Tab. 2.3 the total acquisition times for the most recent DBT systems available in the market are reported.

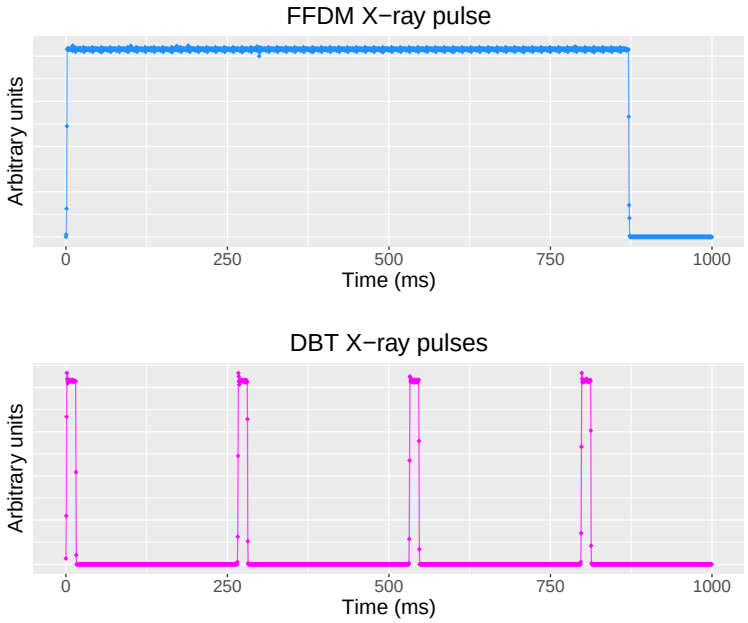

Figure 2.6: Radiation pulses emitted by an X-ray tube, respectively in FFDM and DBT modalities, in a milliseconds timescale.

Mammography system	Scan time (s)
GE Healthcare SenoClaire	7
GE Healthcare Pristina	
Hologic Selenia Dimensions	3.7
Hologic 3Dimensions	3.7
IMS Giotto Class	10
Siemens Mammomat Inspiration	21.8
Siemens Mammomat Revelation	
Fujifilm Amulet Innovality	3.5

Table 2.3: Total acquisition time expressed in seconds, for the most recent DBT systems in the market.

2.5.2 Compressor

Firm, but not painful, breast compression is a necessary part of the mammography examination for several reasons. It forces the various tissues (fat, fibroglandular and cancerous) to stretch, minimizing the superposition from different planes and the overall breast thickness. Typical compressed breast thicknesses lie in the interval of 2-8 cm. The compression plate can be made of polycarbonate or other radiolucent materials that do not severely interfere with the properties of the X-ray beam. Breast compression offers benefits in terms of patient exposure and image quality. The reduced breast thickness provides lower overall attenuation of the incident radiation, thus allowing the reduction of the effective dose, and gives a more uniform attenuation over the image. It is important that the breast is compressed as uniformly as possible and that the edge of the compression plate at the chest wall is straight and aligned with both the X-ray tube focal spot and image detector to maximize the amount of breast tissue that is included in the image. Moreover, the compression allows to decrease the distance from any plane within the breast to the detector, thus lowering the geometric unsharpness, and performs a clamping action, which reduces anatomical motion during the exposure preventing this source of image degradation. The use of the compression plate during the exposure decreases also the amount of scattered radiation that reach the image detector. In fact, the scatter ratio in mammography increases with increasing breast thickness and breast area while is relatively constant with the tube voltage. As in other areas of radiography, scattered radiation degrades the subject contrast, so it must be reduce as

much as possible with some form of scatter rejection.
The compression plate can perform compressions up to 20 daN, even if normally compressions of 5 daN are used for rigid phantoms, while for breasts it would be optimal to reach 13-14 daN. After a certain thickness reduction, the application of additional pressure provides little benefit in terms of image quality and only contributes to patient discomfort. Specialized mechanisms have been introduced by several manufacturers to try to achieve better compression, while minimizing the risk of over-compression.

2.5.3 Anti-scatter grid

The use of an anti-scatter grid, also known as a *Bucky-Potter grid*, can further reduce the fraction of scattered radiation. In the absence of some form of scatter rejection, about 40-50% of the total radiation incident on the detector would have experienced a scattering interaction within the breast tissues. This would be detrimental for the image quality because in addition to subject contrast reduction, the recording of scattered radiation reduces the dynamic range of the detector and adds stochastic noise to the image.
In mammography, it is typical to use focused linear grids that consist of a series of alternating strips of lead and a radiolucent substance such as plastic, carbon fibre, aluminum or even paper. The grid is placed between the patient and the image detector. Its working principle, schematically represented in Fig. 2.7a, is based on the fact that ideally only X-rays that have travelled straight through the patient are able to impinge on the radiolucent septa of the grid and hit the detector. In fact, all the X-rays scattered by the breast tissues are deflected from their original direction, therefore they impinge on the lead strips at different angles, thus being attenuated or further dispersed. As a result, ideally only radiation which has not undergone scattering is imaged on the detector. The most important parameter that influences the performance of an anti-scatter grid is the *grid ratio*, defined as the ratio of the height to the width of the inter-spaces h/d. Higher values of grid ratio correspond to longer septa and thinner inter-spaces. This geometry has both good and bad aspects: the penetrability of the grid is weak, therefore the scattered radiation that reach the detector is greatly reduced but also the primary radiation is attenuated, since it is more likely to impinge on the lead septa rather than on inter-spacers. This effect can be clearly observed in Fig. 2.7b, where the penetration trends for an ideal grid, that should be able to absorb all the scattered X-rays and let to pass all the primary radiation, are

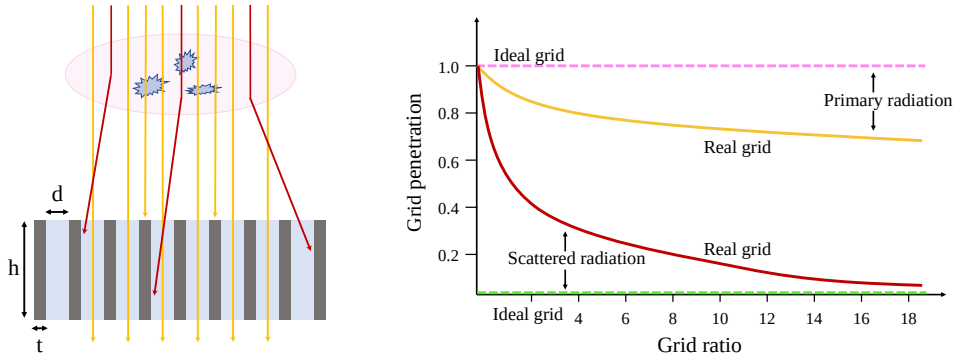

(a) *Working principle* (b) *Penetration property*

Figure 2.7: Scheme of a linear anti-scatter grid working principle and graph of the penetration performance in function of the grid ratio.

reported in pink and green. The yellow and red curves represent the penetrability of a real grid that, depending on its grid ratio, is able to partially attenuate the scattered X-rays and partially transmit the primary radiation. The choice of the grid ratio is a compromise between a good scatter cleanup and an acceptable radiation dose to the patient. It is in fact necessary to compensate for losses of X-ray fluence at the image detector, that are caused by absorption of primary radiation by the septa as well as removal of scatter by the grid. This is reflected in the *bucky factor*, defined as the ratio of radiation on the anti-scatter grid to the transmitted radiation, which can be as large as 2 to 3 in mammography. For this reason, an increase in the tube current is normally required when the grid is used. The improvement in the image quality is generally considered sufficient to justify this increase in dose to the breast. In fact, all the FFDM examinations are performed with the anti-scatter grid. On the contrary, in case of DBT modality, the use of the grid is at the discretion of the manufacturer. The main drawback is linked to the fact that, the use of conventional grids in DBT would result in unacceptable loss of primary radiation, because the motion of the tube forces the X-rays out of the grid septa focus line. To date, only GE Healthcare has developed specific grids for DBT mode with septa perpendicular to the chest wall, instead of parallel as for FFDM one [10]. In more detail the SenoClaire system employs a moving grid with a density of 102 lines/cm and a grid ratio of 5:1 while the Pristina system uses a moving grid with a density of 67 lines/cm and a grid ratio of 11:1.

In modern mammography systems the anti-scatter grid is removable, except in the case of GE Healthcare Pristina. When the anti-scatter grid is used, depending on the manufacturer, different strategies are implemented to avoid the formation of artifacts in the mammogram related to the grid septa. The most common strategy is to constantly move the grid during the X-ray exposure to blur the image of the lead strips. It is important that this motion is uniform and of sufficient amplitude to avoid non-uniformity in the image.

2.5.4 Detector

A radiation detection system can be thought of as consisting of two parts: a *detector*, in which the interaction with the transmitted radiation takes place, and an associated electronic circuit, that acquires the data output from the detector and develops the final image. The most recent mammography systems use digital detectors which can be classified, depending on the detection method, into indirect digital and direct digital detectors. The first consist of a scintillator layer, typically made of thallium activated cesium iodide (CsI), coupled with an electronic light sensor such as an amorphous silicon (a-Si) photodiode or photomultiplier. The other detection method replaces the scintillator with a semiconductor, typically amorphous selenium (a-Se).

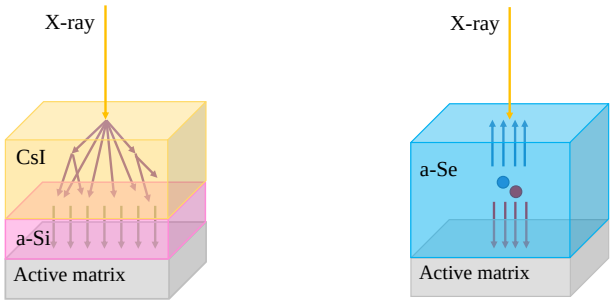

(a) *Indirect* (b) *Direct*

Figure 2.8: Scheme of a detector respectively made of CsI-Si (a), a scintillator material coupled with an electronic sensor, and of a-Se (b), a semiconductor.

In 2.8a, the detection is indirect because the X-ray, transmitted by the breast, interacts in a first step with the scintillator layer, which in turn releases visible light whose intensity is proportional to the incident radiation intensity. This scintillator property is called luminescence. Then, in a second step,

the visible light that reaches the coupled sensor is converted into a usable electric signal. In particular, it is generated a number of electrons proportional to the total amount of incident light photons. For this reason, to avoid any loss of information, it is essential that the absorption spectrum of the light sensor overlaps well with the emission spectrum of the scintillator. The main disadvantage of this type of detector is that the scintillator layer emits the visible light isotropically throughout the space. This means that only a small fraction of the photons would reach the light sensor and most of the signal would be completely lost. For this reason, current breast imaging technology uses structured scintillators made of phosphor crystals that form needle-like elements. In this way it is possible to significantly reduce the lateral spread of visible light, since each crystal acts as a sort of fiber optic directing the light towards the electronic light sensor. In 2.8b, the conversion process is direct because the energy of the absorbed X-ray causes the liberation of electron-hole pairs in the semiconductor, whose number is proportional to the released incident radiation intensity. The charged particles are drawn to the opposite face of the detector, by an externally applied electric field, to collect directly the electric signal. Unlike indirect detectors, the electric field can be tailored to collect the charge with minimal lateral spread. The detection methods just described have a common component: the *active matrix*, as can be seen in Fig. 2.8. This is the key readout method in medical X-ray applications that enables the formation of the digital image from the electric signal, providing the individual control of each pixel through a matrix of Thin Film Transistors (TFTs) and capacitors.

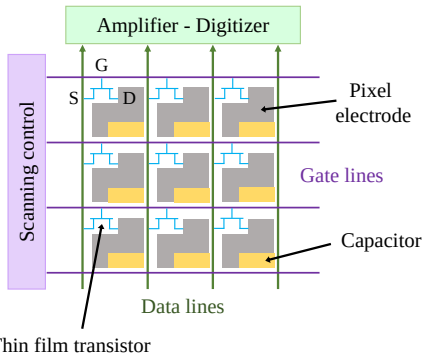

Figure 2.9: Scheme of a TFT active matrix array.

In the side figure, the layout of a group of detector elements, *dels*, on an active matrix arrays is shown. When the image is displayed on a monitor, the individual elements are referred to as image elements, *pixels*, and their value is determined by the information acquired on the corresponding detector element. The size of a del is referred to as the *pixel pitch*. Each del is composed of a thin film transistor switch, a storage capacitor and a pixel electrode. All the switches along a particular row are connected together with a single control line, called gate line.

Mammography system	**Pixel pitch (μm)**	**Detector material**
GE Healthcare SenoClaire	100	CsI-Si
GE Healthcare Pristina	100	CsI-Si
Hologic Selenia Dimensions	70	a-Se
Hologic 3Dimensions	70	a-Se
IMS Giotto Class	85/83	a-Se/CsI-Si
Siemens Mammomat Inspiration	85	a-Se
Siemens Mammomat Revelation	85	a-Se
Fujifilm Amulet Innovality	68	a-Se

Table 2.4: Pixel pitch and detector material of the most recent mammography systems in the market.

This allows the external circuitry to change the state of all the switching elements along the row with a single controlling voltage. Each row of dels requires a separate switching control line. The signal outputs of the dels, down a particular column, are connected to a single data line with its own readout amplifier. The active matrix arrays do not transfer signal between adjacent dels but from the single del directly to the readout amplifier and digitizer, via the data line. This readout system allows the data of all the dels to be read in a fraction of a second. In Tab. 2.4, the pixel pitch and the type of detector of the most recent mammography systems are reported.
It is clear that the incident X-ray information must be sampled in both the spatial and intensity dimensions. Spatially, samples are obtained as averages of the intensity over detector elements, that usually are square and are spaced at equal intervals throughout the plane of the detector. The only exception is the Fujifilm Amulet Innovality system which features hexagonal shaped dels. In mammography, typical pixel pitch should not exceed 100 μm (Tab. 2.4), to avoid the loss of small fundamental details such as microcalcifications. In the intensity dimension, the signal is digitized into a finite number of levels, which are expressed in binary notation as bits. At least 12 bits should be defined for each system. In fact, to avoid degradation of image quality it is essential that the del size and the bit depth are appropriate for the requirements of the imaging task.
The main quality metrics that determine the performance of a detector are the Modulation Transfer Function (MTF) and the Detective Quantum Effi-

ciency (DQE). The first describes the ability of the detector to transfer the contrast of a structure to the final recorded image. It is closely related to the spatial resolution, which determines the dimensions of the smallest visible object. A higher spatial resolution allows better detection of small details in the image, thus improving the visibility and morphological analysis of micro-calcifications. The maximum spatial resolution that can be visualized in an image is defined by the cut-off frequency of the detector, calculated from the pixel pitch. According to Nyquist's sampling theorem, the cut-off frequency of an imaging system is given by:

$$f_{cut-off}(line\ pairs/mm) = \frac{1\ line\ pair}{2 \cdot pixel\ pitch\,(mm)}. \tag{2.1}$$

The visualization of smaller objects requires a detector with a smaller pixel pitch, i.e. with a higher cut-off frequency. The loss of contrast depends on the dimensions of the X-rayed detail, i.e. the spatial frequencies contained in the image between 0 and $f_{cut-off}$ of the detector. The MTF varies between 1 and 0, where 1 corresponds to the complete transmission of the contrast of the object and 0 corresponds to a null transmission, that is the complete loss of visualization of that object. Therefore the MTF is equal to 1 for zero spatial frequency and progressively decreases as spatial frequencies in the image increase up to the $f_{cut-off}$, where it becomes equal to 0.
The DQE characterizes the efficiency of a detector in converting the transmitted X-rays into an image signal. It is generally expressed as a function of the spatial frequency as:

$$DQE(f) = \frac{SNR^2_{out}(f)}{SNR^2_{in}(f)}, \tag{2.2}$$

where SNR is the Signal to Noise Ratio, a measure that compares the level of a desired signal to the level of background noise. The DQE is therefore defined as the ratio of the squares of the SNR at the detector input and detector output. An ideal system, which would use all photons reaching the detector without adding any noise, would have a DQE equal to 1. A real detector always has a DQE smaller than 1 and is increasingly more performing as its DQE approaches 1. The DQE of a system is maximum for zero spatial frequency and decreases with increasing spatial frequencies, due to decreased detector output signal and increased noise. The detective quantum efficiency is improved by using thicker detectors or materials with a

higher attenuation coefficient. It is important to obtain an high DQE value because it improves the image quality without increasing the dose to the patient, or even by decreasing this dose. In fact the digital image quality strictly depends on the SNR, where the signal and the noise are respectively proportional to the total number of photons N_γ collected to form the image and to the square root of N_γ. Therefore the overall SNR can be improved either by increasing N_γ (through a higher mAs value), together with an increase in the dose to the patient, or by maximizing the used portion of the photons reaching the detector. This last condition corresponds exactly to an high detective quantum efficiency. The DQE can also be defined as a function of the MTF as follows:

$$DQE(f) = \frac{MTF^2(f)}{(K_{Dtot} \cdot SNR_{in}^2)\, NNPS(f)}. \tag{2.3}$$

In the previous expression K_{Dtot} is the estimated air kerma at the detector surface and $NNPS(f)$ is the normalized noise power spectrum. In the imaging system, the noise transfer is different from signal transfer and additional noise is added during the detection process from both electronic components and from the intrinsic Poisson variability related to each single electron. The Noise Power Spectrum (NPS) describes the spatial frequency dependence of the noise: it can be thought of as the variance of image intensity distributed among the various frequency components. A normalized noise power spectrum can be conveniently defined as:

$$NNPS(f) = \frac{NPS(f)}{NPS(0)}. \tag{2.4}$$

The NNPS is often assumed to be a constant for a detector, implying that noise transfer is independent of dose. For medium to high doses, this is a reasonable assumption. However, attention should be paid for images recorded under conditions where contributions from the detector readout noise are significant. This readout contribution is not dose dependent and a more robust description of the NPS at low dose requires separation of the NPS into a dose-dependent term, arising from the intrinsic physical noise, and a dose-independent term, arising from the electrical noise. In Eq. 2.3, in the denominator appears SNR_{in}^2 which corresponds to the number of X-ray photons for the beam quality used. SNR_{in}^2 values are tabulated for some typical spectra (with added 2 mm Al at the tube) used by the current X-ray

systems, as provided by IEC 62220-1 [11]. The data of Boone and colleagues [12] can be used to calculate SNR_{in}^2 for spectra that are not included in the IEC standard, using the formula:

$$SNR_{in}^2 = \int \frac{\Phi(E, kV)}{K_a}\, dE, \tag{2.5}$$

where $\Phi(E, V)$ is the photon fluence at energy E and tube voltage kV.
MTF and NPS are sensitive image quality parameters and are sufficient to track changes in detector performance. The DQE is an important image quality metric when comparing the absolute performance of detectors, either of a similar type or between manufacturers. In principle, there are two advantages of direct compared with indirect conversion detectors:
1. The single conversion stage allows to have a significantly higher conversion efficiency of X-ray energy to electric signal on the active matrix, thus providing an higher DQE.
2. The limited lateral spread during the signal (electrons) collection phase allows a much higher spatial resolution. This is reflected in an higher MTF and in the possibility to use thicker detectors to further improve the DQE, without significant reduction in resolution.
Currently in mammography the optimal choice is a-Se: it increases the DQE beyond what is possible with a scintillator and allows a high resolution. Indeed, although technical problems limit its thickness, its low Z is ideally matched to the absorption requirements of low energy X-ray spectra.

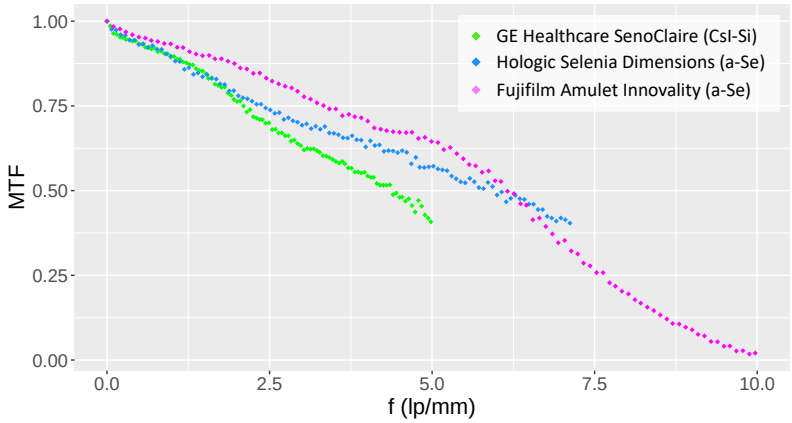

Figure 2.10: MTF of mammography systems with different digital detectors.

In the graph above, it is possible to observe the comparison of the empirically measured MTF values on mammography systems currently in use in the hospitals where I did my internship. It is evident that the worst results are obtained with GE Healthcare SenoClaire, characterized by an indirect CsI-Si detector and by a pixel pitch of 100 μm. Its detector characteristics are less performing than the other systems: both Fuji Amulet and Hologic Selenia use a direct a-Se detector with lower pixel pitch values. In particular, Fuji Amulet provides the best results in terms of MTF and this is due to the fact that the hexagonal shaped dels have a better signal sampling capacity that allow images with pixels of 50 μm to be obtained. These observations are related only to the performance of the detector therefore it is not possible to deduce the 'best' system from this single analysis.

2.5.5 Automatic Exposure Control

The X-ray penetration through the breast depends on its thickness and composition. Thick or dense breasts, if relatively low tube voltages are used, require very long exposure time to achieve adequate signal. This would result in a high dose to the patient and the possible creation of artifacts due to anatomical motion. On the contrary, a more penetrating beam allows a lower dose to be used but causes a loss of image contrast. Since it is difficult to estimate the attenuation of the breast by visual inspection, modern mammography systems are equipped with the *automatic exposure control* (AEC), to set the optimal exposure parameters. The AEC typically consists of an ionization chamber or a solid state detector, positioned underneath the image detector to avoid the formation of shadows on the image.
The automatic exposure control deduces the thickness of the compressed breast, from the position of the compression paddle, and measures the X-ray transmission trough a short pre-exposure. The latter is a low dose image, created in the digital detector, that can be analysed to determine the overall image quality, i.e. the SNR. It gives the opportunity to determine the exposure using information from all areas of the breast. Based on this information, the AEC uses an algorithm to automatically set the optimal exposure conditions for the main image. More in detail, based on the position of the compression paddle, the material of the anode, the filter and the kVp are set, while the mAs are chosen based on the pre-exposure. All systems incorporate appropriate constraints to ensure that equipment operation complies with regulatory radiation dose limits and within the working

functional ranges of the X-ray tube and image detector. During an examination, imaging can be optimized according to a priority of SNR, lower dose, or a combination. Different manufacturers have approached this challenge in different ways and development in this area is still ongoing. For example, the location of the edges of the breast can be segmented automatically so that the algorithm is only sensitive to the region of the image within the breast. The algorithm can also be trained to identify automatically the densest areas, usually in the glandular tissue, that will dominate the selection of exposure parameters. Furthermore, special modes of operation can be developed for specific tasks, such as imaging breasts containing implants.
A mammography system should always incorporate a fully automated AEC. In fact, a system with solely manual exposure control, in which the radiologic technologist has to set manually all the parameters based on the breast thickness and estimated composition, is not acceptable. To date, it is also discouraged the use of a semi-automatic AEC, in which only the exposure time is set automatically and the user has to choose all the other parameters, i.e. anode material, filter and tube voltage. The reason why a fully automated AEC is highly recommended is that it optimizes image quality, preventing problems due to quantum noise caused by underexposure and detector saturation or to high doses resulting from overexposure.

2.6 Digital images in mammography

In mammography, in order to optimize the diagnostic interpretation by improving the visibility of the patient's anatomy, digital image processing is performed. Depending on the type of processing operations applied, different types of images are defined. Furthermore, only in DBT modality, the acquired projections are not only processed but also supplied to dedicated reconstruction algorithms capable of generating focal plane images at different heights. The different types of digital images and the reconstruction algorithms, used in mammography, are described below.

2.6.1 Digital image types

The standard for the communication and management of medical images and related information is Digital Imaging and Communications in Medicine (DICOM). It is a very useful format in the hospital sector because it includes

protocols for image exchange and compression, image presentation and results reporting. Moreover, from each image in DICOM format, it is possible to obtain information relating to the patient, the type of examination, the acquisition methods and the image processing operations, by analyzing the so called *header*. The header, found at the beginning of the image file, is constituted of information fields called *tags* usually encoded by pairs of numbers (XXXX, XXXX), in hexadecimal format.

In FFDM modality there is only one type of image: the two-dimensional projection acquired at "high dose". This presents in the header the tag Modality (0008, 0060) with the attribute MG and the tag Presentation Intent Type (0008, 0068) which admits only two attributes:

1. FOR PROCESSING - it is the type of image whose numerical content is closest to the raw pixel data. This does not mean that the image has not undergone any processing: corrections are applied for the heel effect or for the detector calibration (e.g. gain, offset, etc.), but the pixel values are in any case linked to the dose. It is the type of image suitable for the measurement and calculation of physical quality indices.
2. FOR PRESENTATION - it is the type of image intended for visualization and diagnostic interpretation by the radiologist, ready for presentation on dedicated monitors. The pixel values are no longer related to dose but the overall image quality and visibility are optimized.

In DBT modality there are three different types of image, that can be summarized as:

- Projection images: a series of "low dose" planar images acquired at different tube rotation angle. These are used by the reconstruction algorithms to generate the final pseudo-volumetric image.
- Reconstructed DBT images: a stack of reconstructed focal planes at different height from the breast support table surface. The image stack is typically oriented parallel to the detector plane, with each image separated by 1 mm depth. The number of reconstructed images depends on the displayed height in mm, and thus on the compressed breast thickness. Typically an increased number of planes are reconstructed respect to the compression paddle displayed height.
- Synthesized image: a two-dimensional image obtained from the stack of the reconstructed focal planes. It is similar to the FFDM image but it is characterized by different spatial resolution, blurring and contrast.

Image type	Modality	Presentation Intent Type
Projection image	BPO	FOR PROCESSING/FOR PRESENTATION
Reconstructed DBT image	BTO	FOR PRESENTATION
Synthesized image	MG	FOR PRESENTATION

Table 2.5: DICOM Modality (0008, 0060) and Presentation Intent Type (0008, 0068) tags, for the different image types available in DBT systems.

Mammography system	Projection pixel size (μm)	Focal plane pixel size (μm)
GE Healthcare SenoClaire	100	100
GE Healthcare Pristina	100	100
Hologic Selenia Dimensions	140	95-117*
Hologic 3Dimensions	70	95-117*
IMS Giotto Class	85/83	90
Siemens Mammomat Inspiration	85	85
Siemens Mammomat Revelation		85
Fujifilm Amulet Innovality	150/100†	100-150/50-100†

Table 2.6: Pixel size of projection and focal plane reconstructed images for the most recent DBT systems in the market.
* Variable with compression paddle height
† The first option is for the ST mode, the second one for the HR mode

The DICOM standard [13] for the different image types available in DBT systems is summarized in Tab. 2.5, where the Modality (0008, 0060) and Presentation Intent Type (0008, 0068) tags are also specified.
In projection images the pixel size is usually equal to the detector pixel pitch. This is not the case of Hologic Selenia Dimensions and Fujifilm Amulet Innovality. These perform respectively a 2x2 and 3x3/2x2 binning operation, which results in an increased pixel size. In more detail, the first is characterized by a pixel of 140 μm while the second gives the possibility to carry out the examination in two distinct modes, standard (ST) and high resolution (HR), characterized by different pixel dimensions. In Tab. 2.6, the pixel size of projection images and also of focal plane images are listed for the most recent DBT systems. The focal slices have properties strictly determined by the algorithm used to reconstruct them. The following section presents an overview of the most used reconstruction algorithms in tomosynthesis.

2.6.2 Reconstruction algorithms

Tomosynthesis reconstruction is a multidimensional inverse problem in which the challenge is to estimate an object, starting from a finite number of its projections. In DBT, a pseudo-volumetric reconstruction of the breast is obtained by acquiring "low dose" projection images at different angles of the X-ray tube. The adjective "pseudo" is used because, unlike computed tomography, only limited angular ranges are scanned, so the information remains partial. The traditional tomosynthesis reconstruction algorithm is called *Shift-and-Add*: by properly shifting and adding the projections it allows to focus and reinforce all the objects present at a certain depth and blur out the structures elsewhere. This means that images of focal planes at different heights can be reconstructed from a single dataset of acquired projections. The operating principle of this algorithm can be schematically observed in Fig. 2.11. Its main limitation is related to the fact that, each synthesized image contains traces of the surrounding structures. This results in a reduction in the contrast and visibility. So, it is necessary to develop more efficient deblurring methods.

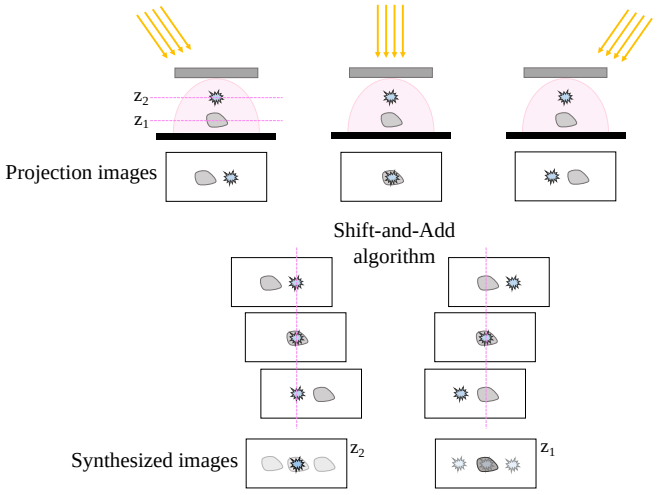

Figure 2.11: Schematic diagram of the Shift-and-Add algorithm in DBT.

Furthermore the Shift-and-Add reconstruction is valid only when the X-ray tube moves linearly, at a fixed height, above the detector [14]. This geometry is typical for chest and body tomosynthesis, while partial isocentric geometry is typically used for DBT. For these reasons many different reconstruction

algorithms have been proposed over the past decades, but only few of them have been widely implemented and used in real-world applications. In breast tomosynthesis, currently existing algorithms can be divided into two main categories: Filtered Back-Projection reconstruction and iterative methods.

2.6.2.1 Filtered Back-Projection algorithms

Filtered Back-Projection (FBP) is the most used algorithm in tomosynthesis. It is derived from CT, in which a large number of projections acquired over 360° (or 180°) are used to reconstruct cross-sectional images. Obviously, due to the limited angular ranges, characteristic of the DBT modality, this algorithm must be suitably modified.
The FBP algorithms are analytical and are based on two mathematical concepts: the Radon transform and the Fourier transform. The first is an integral transform which maps a function $f(\mathbf{r})$, defined on a xy-plane, to a function defined on the two-dimensional space of lines in the plane, whose value at a particular line L is equal to the line integral of the function over that line:

$$Rf(L) = \int_L f(\mathbf{r})|d\mathbf{r}|, \tag{2.6}$$

where Rf is the Radon transform. If $f(\mathbf{r})$ represents an unknown object, then the Rf represents the projection data obtained as the output of a tomographic scan. Hence, the inverse of the Radon transform can be used to reconstruct the original function starting from the projection data, and thus it forms the mathematical basis for the reconstruction. A fundamental role in the FBP theory is also played by the *Fourier slice theorem*, schematically represented in Fig. 2.12. It states that the Fourier transform of a parallel projection of $f(x, y)$ taken at angle θ, gives a slice of the two-dimensional transform $F(u, v)$ subtending the angle θ with the u-axis. In other words, the projection of an object corresponds, through the Fourier transform, to a sampling of that object along the direction perpendicular to the X-ray beam, in the frequency domain. Therefore, with a large number of projections at different angles, the information is well sampled and the object can be reconstructed by combining the data from all the projections. The figure below shows the imbalance of the acquisition density in the frequency domain. The density of the rays in the center is much higher than at the borders. This inhomogeneity is corrected through an appropriate filtering step. In particular, filters are applied to correct the intrinsic effect of the back-projection

of amplifying low-frequency signals and to reduce the intrinsic and statistical noise, linked to the stochastic nature of the radiation. Therefore the FBP reconstruction algorithm consists in performing the Fourier transform of each vector of the Radon space (the space that contains the projection values). The sampled frequency domain is then modified, using appropriate filters, because it requires less time than filtering in real space. The inverse Fourier transform is then calculated returning to Radon space and finally, the back-projections on the modified profiles are computed.
In DBT modality, since the scanned angular range is limited, a large portion of the Fourier domain remains unsampled, as can be seen in the figure below. This is the cause of the anisotropic resolution: despite the excellent in-plane resolution, the lack of a significant amount of information causes a blurry reconstruction in the z-direction.

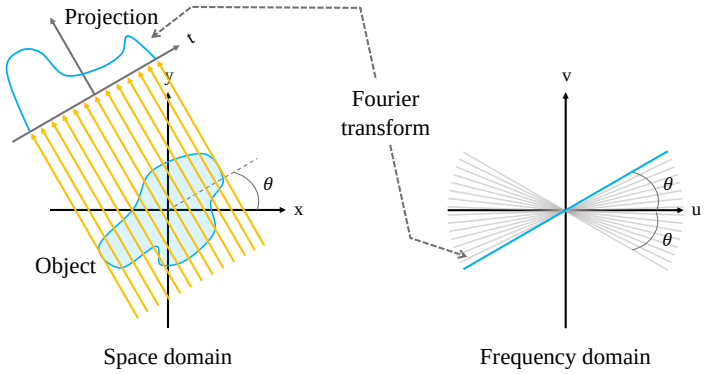

Figure 2.12: Illustration of the Fourier slice theorem and of the portion of the frequency domain sampled by the DBT system.

2.6.2.2 Iterative algorithms

Iterative algorithms refer to an image reconstruction, used in CT and in tomosynthesis, which is obtained by constantly improving the agreement between the pseudo-projections and the empirically measured ones. These techniques are usually computationally more expensive than the common FBP method, which calculates the image in a single reconstruction step. There is a large variety of iterative algorithms, but all of them are characterized by a common procedure: a standard FBP method is used to produce a primary image starting from the raw data, then the iterative steps begin. The

pseudo-projections of the primary image are calculated and compared with the empirically acquired projections. The comparison produces an error matrix, which is used to correct and update the primary image. These steps are repeated iteratively to minimize the error matrix until a predefined threshold is reached or when the maximum number of iterations is reached. At this point the pseudo-projections are back-projected and the reconstructed image is finally obtained. Since the reconstruction of an image from the acquired projections is an inverse problem, very often it is not possible to find exact solutions. Direct algorithms, such as FBP, have to find in a single step approximate solutions which might cause visible reconstruction artifacts in the image. Instead, iterative algorithms approach the correct solution using multiple iteration steps, which allow to obtain a better reconstruction at the cost of a higher computation time. It is important to note that noise is introduced at every attempt to make the simulated image converge to the measured one. For this, an important parameter is the maximum number of iterations that can be performed. A compromise must be reached between an acceptable degree of noise and a satisfactory reconstruction. Iterative reconstruction has undergone notable improvement with the introduction of model-based algorithm. These can embed information related to optics, physics and statistical noise, thus improving the reconstruction performance while keeping the patient dose as low as reasonably achievable, according to the ALARA principle.

Chapter 3

Quality controls of breast tomosynthesis

3.1 Quality control

Quality control (QC) is part of quality assurance, which consists in all those planned and systematic actions necessary to provide adequate assurance that a system, component or procedure will perform satisfactorily in compliance with agreed standards [2]. QC tests of mammography system are aimed at maintaining the patient's exposures as low as reasonably achievable (ALARA principle), while obtaining the highest quality diagnostic information. A routine quality control is necessary to detect degradation over time and it is particularly important when the equipment is used for population screening programs. There are three types of Quality Control tests:
1. Acceptance tests - they must be performed at the time of installation in order to verify compliance with the purchase regarding the technical specifications provided by the vendor. They also determine the characteristic baseline to be used as a reference for subsequent tests and they are used to verify the compliance with the action levels and typical values.
2. Constancy tests - they must be performed periodically to verify that there are no significant deviations from the characteristic baseline.
3. Tests after relevant maintenance - they must be performed after a significant maintenance, such as X-ray tube or filter replacement, detector replacement or software upgrade. Still, the baseline should be used as a reference.
There are specific QC tests for all the components of a mammography system

(see *Section 2.5* for a detailed description of the components). Thanks to these tests, it is possible to verify the correct functioning of each phase of the chain of operations involved in the production of a diagnostic image. In particular, QC tests are defined for the X-ray tube, the AEC, the detector and for the image quality and displays dedicated to reporting. The medical physicist is responsible for the coordination of the quality control of the mammography system, in compliance with the current legislation (2013/59/EURATOM, D.Lgs. 101/20) and with specific international European guidelines and protocols. Constancy QC tests are performed on a six-months or annual basis, but high-frequency checks (daily, weekly, monthly) are also foreseen for monitoring the long-term reproducibility of the equipment. As far as the physical-technical quality and its impact at the diagnostic level is concerned, there is no difference between screening and clinical mammography. For this reason, the QC tests are valid for all mammography systems without further specifications regarding their use. The only difference between the two above-mentioned ways to use a mammography system concerns the QC tests frequency. The equipment used for screening programs requires a six-monthly check while those used for clinical purposes require an annual check. Instead, it is necessary to define specific QC tests for 2D modality, such as FFDM and 3D one, i.e. DBT. Pursuant to D.Lgs. 101/20, the medical physicist must perform quality controls according to the most recent guidelines. To date, the most recent protocols for 2D mammography are EFOMP 2015 [16] and EUREF 2017 (supplement to EUREF 2013 [17]). While for digital breast tomosynthesis the most recent ones are EUREF 2018 [18] and ACR 2020 [19]. As already mentioned, the most recent mammography systems in the market allow to perform the examination in both FFDM and DBT modalities. For this reason, the protocols for breast tomosynthesis simply add some significant QC tests to those traditionally performed in the 2D modality. Due to the different characteristics of the X-ray pulses (2.6), tube loading and anode/filter combinations, it is necessary to repeat also in DBT all the QC tests of 2D modality. The latter have been used for years and are extensively tested while the protocols for 3D modality are recent and are still being optimized. This is why many expert groups [20-23], all around the world, are still working on them. In 2021, Italian medical physicists of AIFM (Italian Association of Medical Physics) formed a working group in order to define an Italian protocol for the quality control of DBT systems. This protocol will reasonably be made public by the end of the current year. The main purposes of the significant QC tests for DBT are described below.

3.2 X-ray tube and dosimetry

All the QC tests described in this section can be performed in the same experimental configuration. In more detail, since images are not needed, it is always recommended to disable the image acquisition or to shield the detector with a protective device, e.g. a lead sheet or lead apron. The measurements can be performed with a calibrated dosimeter, such as an ionization chamber or a solid-state detector, calibrated for clinical beams. From the mammography unit console, it is necessary to select the zero-degree angle stationary tomo mode. This is a peculiar modality, specially developed to facilitate quality control tests, in which all the projection images are acquired with the X-ray tube fixed at the zero angle.

Tube output
The purpose of the tube output QC test is to measure the incident air kerma K_i for different X-ray beam qualities to allow the dosimetric calculation. In radiology, it is often measured the entrance surface air kerma $ESAK$, defined as the air kerma on the central X-ray beam axis at the point where the beam enters the patient. The contribution of back-scattered radiation is included through the back-scatter factor B, thus:

$$ESAK = B \cdot K_i, \tag{3.1}$$

where in K_i only incident radiation is included. The tube output, expressed in units of μGy/mAs, depends on the X-ray beam quality determined by tube voltage, target material and added filtration. It does not have to meet any specific limiting values but it should be stable and consistent during exposures. This QC test should be performed after the replacement of the X-ray tube/filter or the maintenance of the generator.

Tube voltage
The purpose of the tube voltage QC test is to verify the accuracy and the precision of the X-ray tube by respectively evaluating the relative difference between the kVp set on the system and the empirically measured one and the reproducibility of the tube voltage measurements. The X-ray beam quality is one of the primary factors influencing image quality and dose, therefore it is important to test the general performance of the X-ray tube. The accuracy can be tested by measuring voltage values that cover the clinical range while the reproducibility can be evaluated by repeating exposures at a fixed

tube voltage normally used in clinic. This QC test should be performed after the replacement of the X-ray tube/filter or the maintenance of the generator.

Half Value Layer
The purpose of the half value layer QC test is to verify the HVL (see *Section 1.3*), in units of mm Al, for all the clinically used anode-filter combinations to allow the dosimetric calculation. To determine empirically the thickness of aluminum needed to reduce the air kerma by greater than 50% it is possible to use aluminum filters of different thicknesses. The HVL does not have to meet any requirements, it simply characterizes the penetration power of a polychromatic X-ray beam and it determines the radiation quality of the emitted beam along with the tube voltage. This QC test should be performed after the replacement of the X-ray tube/filter.

Average Glandular Dose
The Average Glandular Dose (AGD) is the absorbed dose in the glandular tissue, in a uniformly compressed breast. Glands constitute the most radiosensitive tissue of the breast, therefore the AGD is the reference radioprotection quantity in this radiological sector. Pursuant to D.Lgs. 101/20, the recording of data relating to mammography examinations must provide at least the value of the AGD, expressed in mGy, calculated according to the most recent guidelines. The AGD is derived from the entrance surface air kerma and it is a function of beam quality and breast thickness and composition. If the characteristics of the breast are not known, AGD can be referred to a standard breast. The purpose of the AGD QC test is to calculate the Average Glandular Dose for a range of typical breast thicknesses using the standard breast dosimetry model [25]. The latter relies on the equivalence in attenuation between real compressed breasts and different thicknesses of polymethyl methacrylate (PMMA), an engineering plastic material.
The first two columns of Tab. 3.1 report the equivalence between thicknesses of PMMA and standard compressed breasts. The third column shows the relative glandular fractions considered in the model. It is essential to emphasize that the glandularity is assumed to be uniformly distributed in the breast tissues. This is obviously an approximation of reality. According to the standard breast model the AGD can be analytically derived as:

$$AGD = g\,c\,s\,T\,K_P, \tag{3.2}$$

where g, c, s and T are tabulated conversion factors [25-28], that must be

PMMA plate thickness (mm)	Compressed breast thickness (mm)	Glandular fraction (%)	AGD action values (mGy)
20	21	97	1.2
30	32	67	1.5
40	45	40	2.0
45	53	29	2.5
50	60	20	3.0
60	75	9	4.5
70	90	4	6.5

Table 3.1: Assumptions of the standard breast dosimetry model: equivalence between thicknesses of PMMA and compressed breast. Relative glandular fractions and 2D action levels in terms of Average Glandular Dose.

chosen appropriately. More in detail, the factor g gives the AGD for a 50% glandular breast and is tabulated against breast thickness and HVL. The factor c is a correction based on non-standard glandularity percentages and is tabulated against HVL and breast thickness, for typical breast compositions. The factor s allows for the use of different X-ray spectra and the factor T is the tomo factor, specific for each DBT systems. The factor K_P is the incident air kerma measured on the PMMA surface. The action levels for this QC test in terms of AGD have not yet been defined. For this reason, until precise values are chosen, a possible criterion is to adopt the action levels of 2D mammography. These are listed in the last column of Tab. 3.1. This QC test should be performed after the replacement of the X-ray tube, filter, detector and/or software upgrade.

3.3 AEC

All the QC tests described below include the analysis of the acquired projection images to evaluate the performance of the AEC. The analysis must be performed on the 'for processing' projection image, where exposure parameters are determined by AEC. This corresponds to the first one for almost all systems except the IMS Giotto Class and Siemens Mammomat systems, for which the useful projection image is the second one. The acquisition modality must be set in the fully automatic clinical AEC mode.

AEC performance

The purpose of the performance QC test is to check if the AEC works properly providing sufficient image quality at appropriate dose levels. Signal-To-Noise-Ratio (SNR) is used as a measure of image quality for a series of images of simulated breasts over a clinical range of composition and thickness. This QC test is also performed to determine the exposure parameters needed to evaluate the AGD (see *Section 3.2*). In practice it is not possible to simulate all clinically encountered breast thicknesses and compositions therefore, in agreement with the standard breast dosimetry model, the AEC performance can be measured using PMMA plates with thicknesses between 20 and 70 mm. This QC test should be performed after the replacement of the X-ray tube, filter, detector and/or software upgrade.

AEC response to breast density variations

The purpose of the breast density QC test is to verify whether the AEC system correctly adjusts mAs and/or kV values to achieve the desired target image quality level within the densest area of the breast. Most systems measure the attenuation of the imaged object during a pre-exposure: the areas with highest attenuation, in the clinically relevant part of the image, should determine the exposure factors for imaging. In fact, the AEC should be able to adapt the SDNR of the projection images to the regions with the highest density, usually composed of glandular tissue. This is very important as glands may mask abnormalities and because the risk of tumors is higher in the glandular structures. To empirically simulate local density variations it is possible to consecutively add, to a uniform PMMA block, small PMMA plates with an aluminum filter. The latter composition allows to represent an area with progressively greater glandularity. This experimental configuration is schematically represented in the side figure.

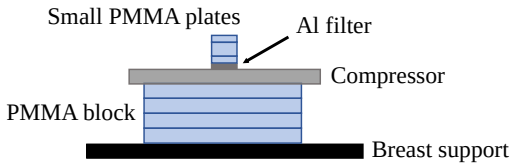

Figure 3.1: Experimental configuration for local dense area QC test.

The typical action levels for this QC test consist of assessing whether mAs, at a fixed kVp value, and AGD increase along with the thickness of the small PMMA stack. This QC test should be performed after the replacement of the detector and/or software upgrade.

AEC short term reproducibility
The purpose of the short term reproducibility QC test is to verify the stability of the AEC. Especially in the screening phase it is important that the different clinical images of a patient are comparable to each other. For the mammography system this means that the AEC should always give similar exposures if the same object is imaged and that the perception and quality of the images should be similar. Therefore it is possible to empirically evaluate the stability of the AEC by consecutively exposing the same PMMA slab repeatedly. This QC test should be performed after the replacement and/or calibration of the detector.

AEC long term reproducibility
The purpose of the long term reproducibility QC test is to verify the stability of the AEC over time in terms of exposure parameters, signal and dose. Due to degradation or malfunctioning of a mammography system, a decrease in image quality might occur. This could negatively affect the visibility of structures in clinical images and change the perception of details. For these reasons it is good practice to keep track of the exposure settings and SNR values by periodically exposing the same PMMA plate over time. The typical action level for this QC test is that the target/filter combination and kV value should remain the same. This QC test should be performed with a weekly and monthly frequency and after the replacement of the X-ray tube/filter, detector and software upgrade.

3.4 Detector

All the QC tests described below include the analysis of the detector performance to assess its impact on the imaging process. In analogy to the typical controls of 2D digital mammography, it is essential to quantify the efficiency with which the detector, together with any associated electronic circuit, converts the incident radiation transmitted by the breast into an electronic signal. The analysis must be performed on the first 'for processing' projection image. The latter in these QC tests is always suitable, regardless of the system, because in manual mode (in the absence of a pre-exposure) the total mAs are evenly distributed across all projections. Furthermore, the use of the first image limits the influence of lag and ghosting.

Response function
The detector response function describes the relationship between the X-ray signal at the detector input plane and the pixel value (PV) generated in the digital image. The purpose of the response function QC test is therefore to establish the relationship between the average PV, in the first FOR PROCESSING projection image, and the air kerma per projection at the detector input plane K_D. The response function is characterized by a model function that is fitted to the data. This is typically linear although other functions are sometimes used, such as the logarithmic one. To fit the appropriate model function (linear or logarithmic):

$$PV = a\,K_D + b \quad or \quad PV = a\,ln(K_D) + b, \tag{3.3}$$

it is necessary to plot the average PV in function of the measured K_D. The fit coefficients a, b can be used to track the detector response function over time. The typical action level for this QC test is that the model function should be monotonic and the fitted function should describe the measured data well. This QC test should be performed after the replacement of the detector or software upgrade.

Noise analysis
The purpose of the noise analysis QC test is to establish the relative fraction of the different noise sources as a function of K_D and to confirm that quantum noise constitutes the highest component of image noise under typical clinical conditions. In a digital image, using a simplified model, it is possible to decompose the total variance σ^2 into three sources: the electronic noise e, the quantum noise q and the structure noise s. These components can be isolated using a weighted polynomial curve fitted to the variance plotted as a function of the incident air kerma per projection at the detector plane [17]:

$$\sigma^2 = e + q\,K_D + s\,K_D^2, \tag{3.4}$$

The noise fit coefficients can then be used to track the X-ray detector noise components over time. The coefficient q can also be used to calculate the quantum noise variance as a percentage of the total variance. The typical action level for this QC test is that the quantum noise must be the largest noise component over the range of clinical detector input air kerma values. This QC test should be performed after the replacement of the detector.

Modulation Transfer Function
The purpose of the modulation transfer function QC test is to quantify the MTF (see *Section 2.5.4*), in projection images. This is important because the latter constitute the input dataset of the reconstruction algorithms that generate the DBT focal planes. The main sources of blurring in the projection images, acquired in fully automatic clinical AEC mode, are the focal spot size, the focal spot motion and the detector MTF. The latter includes the effect of blurring due to the X-ray converter, pixel size and detector binning. More in detail, in the tube travel direction the MTF may be strongly influenced by the tube motion, which in turn depends on the exposure pulse length per projection image. The degree of blur, due to focal spot size and motion, depends on the height above the breast support table, therefore the MTF should be evaluated at different heights above the breast support table, corresponding to a range of real compressed breast thicknesses, by imaging the dedicated MTF edge test device. This QC test should be performed after the replacement of the X-ray tube, filter and/or detector.

Detector element failure
The purpose of the element failure QC test is to check that the interpolation of pixels, corresponding to non-functioning dels, does not cause the onset of artifacts that could potentially limit a correct diagnosis. In fact, in the event of a malfunctioning del, there are specific algorithms capable of obtaining the value of the corresponding (bad) pixel by interpolating the values of a finite set of adjacent pixels. The dels for which values have been interpolated are listed in a *bad pixel map*. This QC test should be performed after the replacement of the detector.

Uncorrected defective detector elements
The purpose of the uncorrected defective elements QC test is to assess the presence and position of pixels associated with malfunctioning dels that have not been included in the *bad pixel map*. The latter are called uncorrected defective detector elements and their corresponding pixel values are not interpolated. These bad pixels can be easily investigated by analyzing images of uniform objects because of their deviating values. The typical action level for this QC test is that no pixels, associated with uncorrected defective detector elements, should be visible. This QC test should be performed after the replacement of the detector.

3.5 Image quality

In digital breast tomosynthesis the Image Quality (IQ) is the quantity used to express the visibility or the interpretability of different breast details, in 'for presentation' reconstructed images, that allow a radiologist to perform a good diagnosis. In the context of QC tests, it is better to talk about *technical image quality*, i.e. IQ parameters evaluated on images obtained by exposing dedicated phantoms. The latter are simplified models of clinical reality that present a set of known details, which simulate real anatomical and pathological breast features. Each phantom has its own specific characteristics but, in general, they all have at least one of the three main types of detail inserted into a uniform background: these are fibers, specks or microspheres and masses, that simulate real breast fibrous structures, microcalcifications and tumors. It is reasonable to assume that improvements in technical image quality are likely to lead to benefit in clinical reality but it is very difficult to establish an acceptable level of diagnostic image quality based on the action levels of the IQ parameters. To date, the image quality represents the most deficient section of the DBT protocols, in fact, all the QC tests described in this section are not yet characterized by action levels or typical values.

Stability of image quality in the x-y plane
The purpose of the x-y plane IQ QC test is to verify the stability over time of the image quality in the reconstructed focal planes and in the synthesized images. As there are still no detailed procedures for assessing IQ in DBT, for the moment it is sufficient to trace its trend over time and verify any significant deviation from the characteristic baseline. The physical evaluation of the visibility of the details in the slice in which they are in focus, based on an a-priori knowledge of the phantom content, could consist into defining measurable objective indices or visual scoring methods. The first approach allows to define objective IQ parameters, such as SNR, SDNR, CNR, with which it is possible to quantitatively evaluate the degradation of IQ over time and also compare the performance of different mammography systems. The second approach consists in assigning predetermined scores for each type of detail, according to how clearly it is visualised. Also in this case it is possible to compare IQ performance over time but the evaluation is not objective: two different observers may not agree on the score. This makes the latter method less robust. This QC test should be performed after the replacement of X-ray tube/detector, clinical AEC mode change or software upgrade.

Z-resolution
The purpose of the z-resolution QC test is to quantify the resolution in the z-direction, i.e. the signal spread of an object between reconstructed planes. Although tomosynthesis reduces the problem of tissue overlap, typical of digital 2D mammography, there is still some inter-plane diffusion of structures that could obscure details of interest. This is linked to the limited angular range of acquisition which allows only a pseudo-reconstruction of the volume: during the examination, the information remains partial and there is insufficient data to localize the breast structures with respect to their height above the support table. As a result, the signal generated by a detail appears in the in-focus plane but also in the adjacent ones, potentially obscuring interesting structures. The signal spread along the reconstructed focal planes can be quantified using the Artifact Spread Function (ASF) which describes the signal profile of a small object, typically a sphere embedded in a dedicated phantom, on a uniform background. There are several ways to define the mathematical expression of ASF but, in general, it depends on the relationship between the intensity of the signal that the detail generates in an out-of-focus plane and the intensity that it generates in the in-focus plane. To quantify numerically the signal spread with an index it is possible to consider the Full Width at Half Maximum (FWHM) of the ASF profile. This QC test should be performed after the replacement of the detector and/or software upgrade.

Homogeneity and artifact evaluation
The purpose of the homogeneity and artifact QC test is to verify, in the DBT reconstructed focal planes and in the synthesized images, the potential presence of inhomogeneities and artifacts. The latter, in fact, could affect the visibility of breast structures in the clinical mammography images thus limiting a correct diagnosis. Homogeneity can be empirically investigated by exposing a uniform block of PMMA. The relative image can be considered homogeneous if it is characterized by approximately equal PV and standard deviation (SD) over the whole area. In parallel, the presence of artifacts can be investigated visually or by measuring the variance: an artifact-free image has no high variance regions. This QC test should be performed after the replacement of X-ray tube/detector, clinical AEC mode change or software upgrade.

Chapter 4

Materials and methods

In this thesis work, the z-resolution, one of the parameters that characterize image quality in DBT, is experimentally evaluated in clinical reconstructed images. As described in *Section 3.5*, the resolution along the z-axis is studied in terms of ASF, which can be quantified numerically through its FWHM. This chapter describes the instrumentation and the empirical approach used.

4.1 Phantoms

The experimental measurements were performed with recent phantoms dedicated to the DBT modality together with 2D digital mammography phantoms, as proposed by [19]. The latter were chosen based on their content because small details, such as specks, are required to analyze the z-resolution.

CIRS Model 015
The CIRS Model 015 produced by the *CIRS Tissue Simulation & Phantom Technology* company is visible in Fig. 4.1a. The phantom is a 44 mm thick square-shaped PMMA block that simulates a 42 mm compressed breast of average glandular/adipose composition. It presents 5 groups of Al_2O_3 specks, each characterized by a different size ranging from 0.16 mm to 0.54 mm.

CIRS Model 011
The CIRS Model 011 produced by the same company as the phantom described above is visible in Fig. 4.1b. The phantom is a 45 mm thick breast-shaped epoxy resin block, a CIRS material that mimics the photon attenua-

tion coefficients of a range of breast tissues. It presents 12 groups of $CaCO_3$ specks, each characterized by a different size ranging in 0.13 - 0.40 mm.

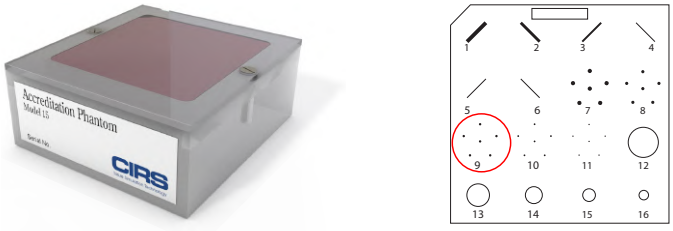

(a) *Model 015*

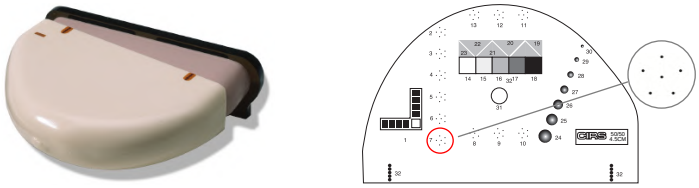

(b) *Model 011*

Figure 4.1: CIRS phantoms used for this thesis work.

Modular DBT Phantom

The Modular DBT Phantom produced by the *Sun Nuclear* company is visible in Fig. 4.2a. Its main peculiarity is the flexible design, since it includes different modules that can be assembled in several ways to evaluate image quality and a wide range of performance metrics. In this thesis work, the chosen experimental configuration consists of a total thickness of 45 mm obtained by superimposing the 15 mm thick Image Quality module on a 30 mm thick Breast Blank module. The latter is an epoxy resin-based uniform block that mimics a 50% glandular and 50% adipose breast. The Image Quality module presents 6 groups of Al_2O_3 specks, each characterized by a different size ranging from 0.14 mm to 0.33 mm.

Tomophan

The Tomophan phantom produced by the *The Phantom Laboratory* company, schematically represented in Fig. 4.2b, is comprised of two PMMA components: the Test Object and Tissue Spacer, for a total thickness of 42 mm. The details of interest for the analysis of the z-resolution are three

Al microspheres with size of 0.5 mm, vertically spaced 10 mm apart, thus covering a total of thickness of 20 mm.

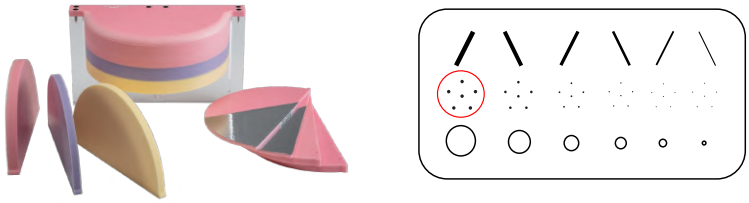

(a) *Modular DBT Phantom and Image Quality module.*

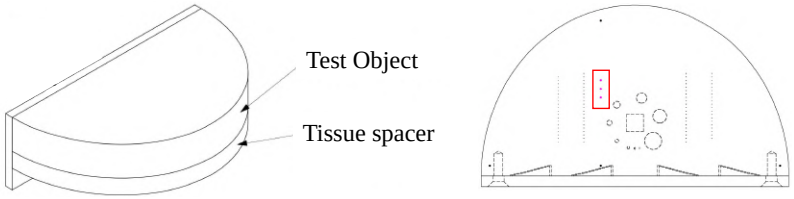

(b) *Schematic representation of the Tomophan phantom.*

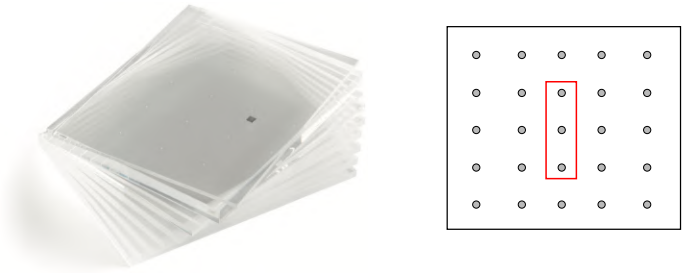

(c) *Pixmam phantom.*

Figure 4.2: Phantoms, dedicated to the DBT modality, used in this work.

Pixmam - 3D

The Pixmam - 3D, produced by the *Leads Test Object* company, has been designed according to EUREF [17], for the quality controls of DBT systems. The phantom comprises various PMMA plates of different thicknesses, as can be seen in Fig. 4.2c, one of which containing 25 embedded Al spheres of 1.00 mm size. The experimental configuration, chosen for this dissertation work, consists of a total thickness of 50 mm obtained by superimposing a 35 mm thick PMMA stack, the slab containing the details characterized by a thickness of 5 mm and an additional 10 mm thick PMMA plate.

The most important characteristics, for the evaluation of the ASF, of all the phantoms described above are summarized in the following table. Specifically, the first rows report the type, material, diameter and height above the breast support table of each detail, chosen to perform the analysis, while the last row shows the total heights of the phantoms.

	CIRS 015	**CIRS 011**	**Modular**	**Tomophan**	**Pixmam**
Details	specks	specks	specks	spheres	spheres
Material	Al_2O_3	$CaCO_3$	Al_2O_3	Al	Al
Diameter (mm)	0.32	0.40	0.33	0.50	1.00
Detail height (mm)	37	23	37	18-28-38	37
Total thickness (mm)	44	45	45	42	50

Table 4.1: Characteristics of the phantoms used for the z-resolution analysis.

4.2 DBT systems

The images of the phantoms were acquired on various mammography systems, all currently in use in hospital facilities in our country. Their most important characteristics are already described in detail in *Chapter 2*. The following table summarizes for each model the number of systems used and the type of reconstruction algorithm implemented.

Mammography system	**Number**	**Reconstruction algorithm**
GE Healthcare SenoClaire	1	Iterative
GE Healthcare Pristina	4	Iterative
Hologic Selenia Dimensions	9	FBP/Iterative
Hologic 3Dimensions	1	FBP/Iterative
IMS Giotto Class	2	Iterative
Siemens Mammomat Inspiration	2	Iterative
Siemens Mammomat Revelation	1	Iterative
Fujifilm Amulet Innovality	4	FBP or Iterative

Table 4.2: Number of DBT systems used for each model and type of reconstruction algorithm implemented.

To date, all the reconstructed images are obtained with totally iterative approaches with the exception of Hologic which has developed a hybrid algorithm based on the FBP method, coupled with an iterative contrast optimization. Fujifilm Amulet Innovality systems are available in two different versions that implement an iterative approach or the FBP reconstruction method, respectively. In this work, only one of the four systems used is iterative. Among all, only Siemens Mammomat systems allow the user to choose an iterative algorithm from several possibilities. In this work the Empire RPG3 was used because it was present in all the systems tested.

4.3 Experimental setup

The images, in all the various DBT systems, were acquired in the same experimental configuration. The phantoms were placed on the chest wall side of the breast support table and the compression paddle, characterized by a size of 24 x 30 cm^2, was positioned exactly at the phantom thicknesses, summarized in the last row of Tab.4.1. The exposures were performed by setting the clinical DBT modality, with moving tube, together with the fully automatic AEC mode. In this way the user does not have to manually set any acquisition parameter, therefore exposure parameters may differ between different DBT systems. This should not affect the z-resolution as it is not influenced by the dose. A photograph of the experimental setup in the case of the Tomophan phantom in the Hologic Selenia Dimensions system, currently in use at the Santa Maria delle Croci hospital, is shown below as an example.

Figure 4.3: Example of the experimental setup.

4.4 Z-resolution analysis

4.4.1 Artifact Spread Function

The mathematical expression of the ASF, used in this work to express the signal spread in a reconstructed focal plane z, is [19]:

$$ASF(z) = PV^{M}_{detail}(z) - \overline{PV}_{bg}(z), \tag{4.1}$$

where PV^{M}_{detail} is the maximum PV that the detail generates in z and $\overline{PV}_{bg}$ is the mean PV of the background in the same plane. The evaluation of the ASF in all the reconstructed focal planes allows to obtain the total profile of the signal spread generated by the detail of interest, i.e. the z-resolution. The FWHM is calculated on the ASF values normalized to the interval [0,1], as:

$$ASF_{norm}(z) = \frac{ASF(z) - MIN(ASF)}{MAX(ASF) - MIN(ASF)}. \tag{4.2}$$

The two quantities $MIN(ASF)$, $MAX(ASF)$ are defined on the overall profile of the ASF. According to Eq. 4.2, a value of $ASF_{norm}(z_f) = 1$ is expected at the focal plane z_f in which the detail is in focus. Ideally all the other adjacent planes should have a null ASF value but in reality the signal diffuses, due to the limited angular range of acquisition typical of tomosynthesis.

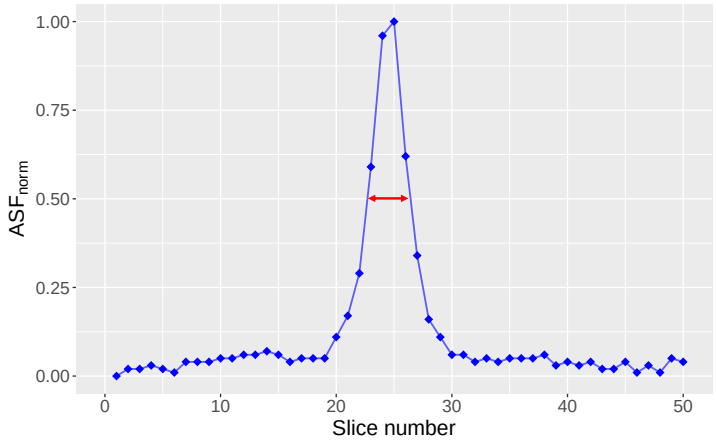

Figure 4.4: Example of an experimental ASF profile.

The previous figure shows an example of a real normalized ASF profile, with the relative FWHM highlighted in red. The FWHM values are always expressed in mm because the depth of the voxels, i.e. the distance between consecutive reconstructed slices, is 1 mm for any DBT system tested.

4.4.2 Image analysis

The z-resolution was always evaluated on the 'for presentation' reconstructed DBT images. The quantitative analysis of the pixel values, both of the signal and of the background regions, was performed using the ImageJ software. In detail, for each area of interest in the image it is necessary to define a ROI on which ImageJ is able to calculate several quantities, such as the area, the maximum and mean grey value, etc. Based on the phantoms used, two different arrangements of ROIs were defined to calculate the ASF.

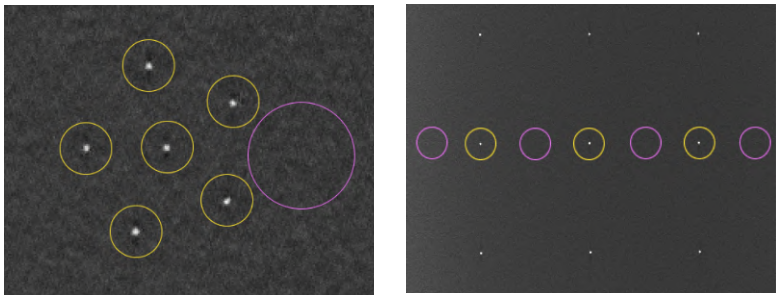

(a) *Detail: specks* (b) *Detail: spheres*

Figure 4.5: Arrangements of the regions of interest in the phantoms used.

For CIRS Model 015, CIRS Model 011 and Modular DBT Phantom, all characterized by groups of 6 specks arranged in the shape of a star, a circular ROI was defined for each single detail and for the background. The layout is visible in Fig. 4.5a where a group of specks, on the DBT plane where they are in focus, is shown. In this case, the ASF expression is computed considering the term PV^{M}_{detail} as the average of the maximum pixel values obtained in the ROIs defined on each speck. For Tomophan and Pixmam, both characterized by three consecutive spheres, a circular ROI was defined for each detail and for all background regions adjacent to the spheres. Again, the arrangement is visible in Fig. 4.5b where the Pixmam details are shown, as an example, in their focal plane. For each sphere, the average between the

mean PV of the two closest background ROIs is used as $\overline{PV}_{bg}$ in the ASF expression. Unlike the previous case (4.5a) in which a single ASF is obtained for the entire group of specks, this latter arrangement of ROIs allows to obtain the signal spread of each sphere. The reason why ASF is evaluated differently depending on the type of detail is that spheres are included in the phantoms specifically for the z-resolution evaluation, while specks are not. In fact, the phantom manuals state that their presence is useful in determining whether the mammography system under study is able to make visible small structures that are critical for early detection of breast cancer. The diameter of the specks is known in the x-y plane but the manuals do not specify their size along the z-axis. For this reason, an alternative approach is proposed in which the pixel values of the signal are averaged over the entire group and not calculated on individual details. It is interesting to try to include specks in the experimental evaluation of the z-resolution because public hospitals more often have phantoms with this type of detail, rather than new phantoms with dedicated spheres.
In addition, the determination of the ASF profile for each individual sphere allows to verify a possible dependence of the signal spread on the spatial position of the detail along the z-axis, in the Tomophan phantom, and in the x-y plane, in the Pixmam phantom. This evaluation would not be significant in the case of specks because the details of a group appear at the same height and very close together, with distances on the order of few millimeters.

4.4.3 Preliminary study

The dimensions and spatial positions of the regions of interest were chosen on the basis of preliminary studies conducted on all phantoms and different DBT systems. The two terms that appear in the ASF expression, according to Eq. 4.1, are the maximum PV of the signal generated by the detail of interest and the mean PV of the background. The mean PV dependence on the size and spatial position of the ROI was studied in 6 background regions, ranging from 0.45 mm^2 to 15.20 mm^2, defined in different positions with respect to the details. In Fig. 4.6, reported below, the ROIs used in the case of a group of specks and of a sphere are respectively shown. The maximum PV dependence on the size of the ROI was investigated across 6 signal regions with different areas, ranging from 0.14 mm^2 to 4.53 mm^2 for a speck and from 0.72 mm^2 to 15.02 mm^2 for a sphere, respectively. Again, the ROIs used for both types of details are shown below in Fig. 4.7.

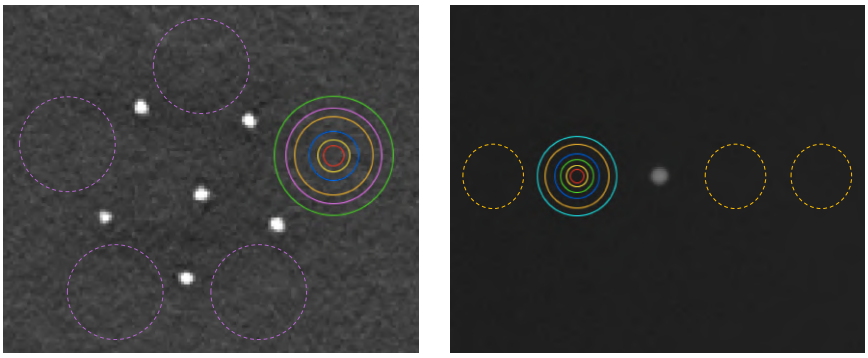

(a) *Detail: specks* (b) *Detail: spheres*

Figure 4.6: Study on the size and spatial position of the background ROI.

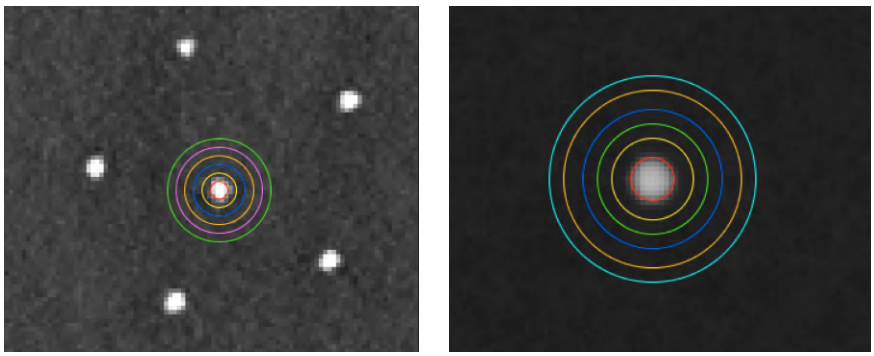

(a) *Detail: specks* (b) *Detail: spheres*

Figure 4.7: Study on the size of the signal ROI.

4.4.4 Repeatability and reproducibility

To test the repeatability of the experimental measurements the exposure of each phantom, in a given mammography system, was repeated three times consecutively. For any DBT system-phantom configuration the FWHM is therefore expressed as the arithmetic mean $\bar{x}_i$ of the three different experimental values, with an associated error equal to their standard deviation σ_i. To test the reproducibility of the measurements, DBT systems of the same model, located in different hospital facilities in our country, were used to expose the same phantoms. In this case, for any DBT system-phantom con-

figuration the characteristic FWHM value is presented as the weighted arithmetic mean of the means, assuming the reciprocal of the squared standard deviations as weights:

$$\bar{x} = \frac{\sum_1^n w_i \bar{x}_i}{\sum_1^n w_i}, \quad with \quad w_i = \frac{1}{\sigma_i^2}. \tag{4.3}$$

The uncertainty associated to $\bar{x}$ is:

$$\sigma = \frac{1}{\sqrt{\sum_1^n w_i}}. \tag{4.4}$$

Chapter 5

Experimental results

In this chapter the experimental results, obtained with the different phantoms and digital breast tomosynthesis systems, related to the evaluation of the z-resolution are presented and discussed.

5.1 Preliminary study

The effect on the FWHM, of the size of the maximum PV of the signal and the size and spatial position of the mean PV of the background, is the same in all the cases analyzed, so a general discussion will be presented. In particular the results obtained with the CIRS Model 011 and Pixmam phantoms in GE Healthcare Pristina, Hologic Selenia Dimensions and IMS Giotto Class systems, are reported as examples. These three DBT systems were chosen because they have different pixel values (see Tab. 2.6) that cover the range of possible sizes that characterize the current mammography systems, while the two phantoms were chosen because they present the largest details.
The *mean PV* is slightly sensitive to both size and spatial position, when considering very small background regions. This effect is linked to the intrinsic noise that affects the value of each pixel in the image. The only way to limit this phenomenon is to calculate the mean PV over larger regions. This is always supported by the empirical results, even in the DBT systems most affected by noise. In fact, in any DBT system-phantom configuration analyzed, it is sufficient to consider areas of few mm^2 to obtain a constant mean PV value as the size and position of the background ROI varies. By fixing a region for the detail, in order to avoid any effect related to the choice

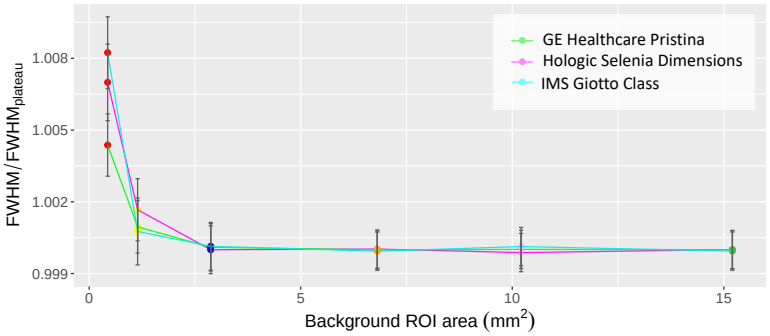

(a) *Detail: specks*

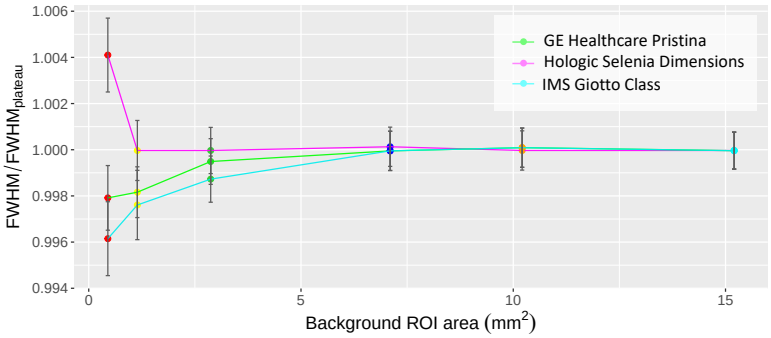

(b) *Detail: spheres*

Figure 5.1: Empirical dependence of the FWHM on the size of the background ROI in an image of CIRS Model 011 (5.1a) and Pixmam (5.1b).

of the signal ROI, it is shown that the FWHM is not affected by the size of the background region, if a sufficiently large area is considered, as it rapidly reaches a plateau. This can be observed in the figure above, which shows the typical dependence of the FWHM, normalized by the corresponding plateau value, on the size of the background ROI observed in each image in all DBT systems. Each experimental point represented is colored according to the corresponding region of interest (see Fig. 4.6). In detail, Fig. 5.1a, 5.1b report the case of a group of specks of the CIRS Model 011 and of a sphere of the Pixmam respectively. By choosing an area large enough to eliminate the dependence of the mean PV on ROI size, it was found that the dependence on spatial position also disappears. This is because the local variations that might characterize the pixel values of a small area, when averaged over sufficiently large regions, are not significant. Notably, all the ROIs represented

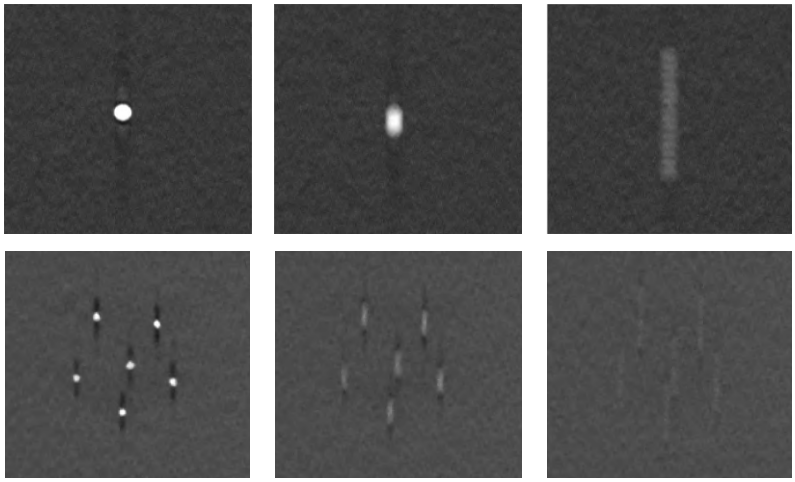

Figure 5.2: Example of the signal spread of a sphere and a group of specks in the direction of motion of the tube. First column in focus planes; second column 5 mm from in focus planes; third column 15 mm from in focus planes.

as dashed curves in Fig. 4.6 were empirically tested. The analysis yielded, for both types of details, a maximum spread of less than 0.1%, i.e. FWHM values that were always consistent with each other. In Fig. 4.6, all the spatial positions of the background regions are defined in the direction orthogonal to the movement of the X-ray tube. The reason is that in the other direction it is possible to find artifacts or blurring due to the motion of the tube itself. In addition, it is always a good practice to define the background ROI at some distance from the detail because it has been observed experimentally that, in most of the DBT systems, the spatial position of the signal changes also in the x-y plane, as the slice considered varies. Again, the translation of the detail is increasingly evident in the direction of the X-ray tube motion as shown in Fig. 5.2, where the typical signal spread of a sphere and of a group of specks between slices in the x-y plane is illustrated as an example. If the latter effect is neglected, an unexpectedly high FWHM value is likely to be obtained because the corresponding background region contains part of the signal generated by the detail in the out-of-focus slices. In the z-resolution analysis a background ROI of 15 mm^2 was used for both types of details. In the case of specks, the spatial position is defined just outside the group, while, in the case of a sphere the ROI is positioned next to the detail in the direction orthogonal to the tube motion (see Fig. 4.5).

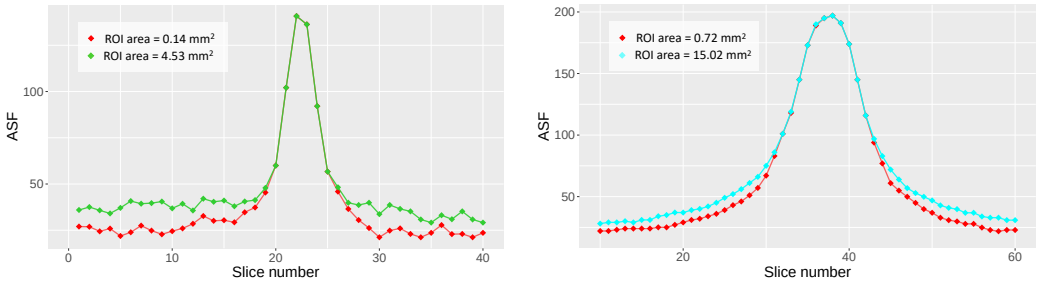

(a) *Detail: specks* (b) *Detail: spheres*

Figure 5.3: Artifact Spread Function profiles for different signal region sizes.

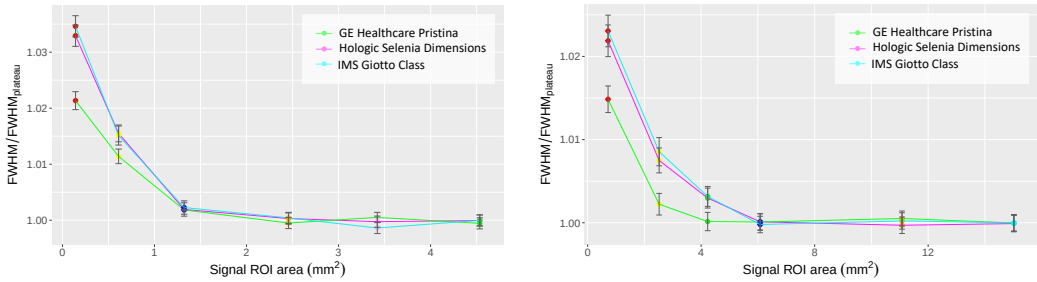

(a) *Detail: specks* (b) *Detail: spheres*

Figure 5.4: Empirical dependence of the FWHM on the size of the signal ROI in an image of CIRS Model 011 (5.4a) and Pixmam (5.4b).

The *maximum PV* of the signal, in the focal plane, is not affected by the size of the ROI as the speck/sphere, in the absence of any disturbing artifact, provides the highest grey level. The only limitation is that the region must completely contain the detail also in the adjacent reconstructed slices. Therefore the ROI must always be larger than the detail of interest, otherwise it is possible to lose significant pixel values in the planes not in focus, as a result of the signal translation in the x-y plane. This could lead to an overestimation of the FWHM, as can be seen in Fig. 5.3 where the non normalized ASF profiles, obtained for the smallest and largest tested signal ROIs, are empirically shown for a CIRS Model 011 and a Pixmam image. The background region used to perform the analysis was defined based on the findings of the preliminary study discussed above. In detail, the profiles obtained with the Hologic Selenia Dimensions are shown as examples (the same effect

was found in all the DBT systems). It is evident that the smaller ROIs (red curves) provide lower tails, in the reconstructed unfocused slices, due to the fact that the maximum PV of the signal is lost and the difference with the mean PV of the background is therefore smaller. During the renormalization process, the red curves are 'stretched' less than those corresponding to the larger ROIs, thus providing broader profiles, i.e. higher FWHM values. This effect is very slight when looking at the corresponding normalized ASF profiles, but it is clearly noticeable also in Fig. 5.4 where the dependence of the FWHM, normalized by the corresponding plateu value, on the size of the signal ROI is shown for an image in the different DBT systems. Each experimental point is colored according to the corresponding signal ROI (see Fig. 4.7). The trend of the FWHM is the same in both phantoms and, in detail, it is characterized by a continuous decrease until a plateau is reached for sufficiently large signal regions. The same behavior was found experimentally with each type of mammography system tested. Based on the results obtained from this study, it is possible to define a valid signal ROI size for each type of phantom used. Among all the phantoms that contain groups of specks the CIRS Model 011 has the largest size of analyzed detail, therefore a signal ROI of 3.5 mm^2, deduced from the empirical trend in 5.4a taking into account the results of all the DBT systems tested, is also valid for the other phantoms. Following the same reasoning, for the Pixmam an area of 15 mm^2 is chosen. The latter is much larger than the ROI defined for the specks for two main reasons. The first one is that the spheres are very isolated so it is possible to define a big ROI without interfering with other signals. In addition, Pixmam spheres are twice the size of the details of all the other phantoms. The second reason is practical, as it is very convenient to have the same ROI for both the signal and the background. Since the spheres of the Tomophan phantom are exactly half of those of the Pixmam, the ROI size deduced from the empirical trend in 5.4b, taking into account the results of all the DBT systems tested, is also valid for them.

5.2 Repeatability of the measurements

The repeatability of the measurements, for all the 5 phantoms used, was tested in the Hologic Selenia Dimensions system, currently in use in Ravenna at the Santa Maria delle Croci hospital, where I did my internship. Other repeatability measures are available, but not for all the DBT system-phantom

combinations tested. The reason is that the used mammography systems, being located in hospitals, are not dedicated to research purposes and very often the time in which they are left available is not sufficient to perform multiple acquisitions, so phantoms need to be exposed only once. In many cases several systems of the same model (see Tab. 4.2) were tested from different hospitals so, in order not to specify the structure of origin, each system is distinguished on the basis of a number associated with its commercial name. The repeatability is calculated as the ratio of the standard deviation of the three FWHM values, obtained from the empirical measurements in a given system, to their arithmetic mean. The related data, available in the various DBT systems for the 5 tested phantoms, are presented in Fig. 5.5, shown below, in percentage form. The repeatability of the measurements for the Pixmam phantom is not illustrated as it was tested in a single DBT system, the Hologic Selenia Dimensions 1, giving a percentage value of 2%.

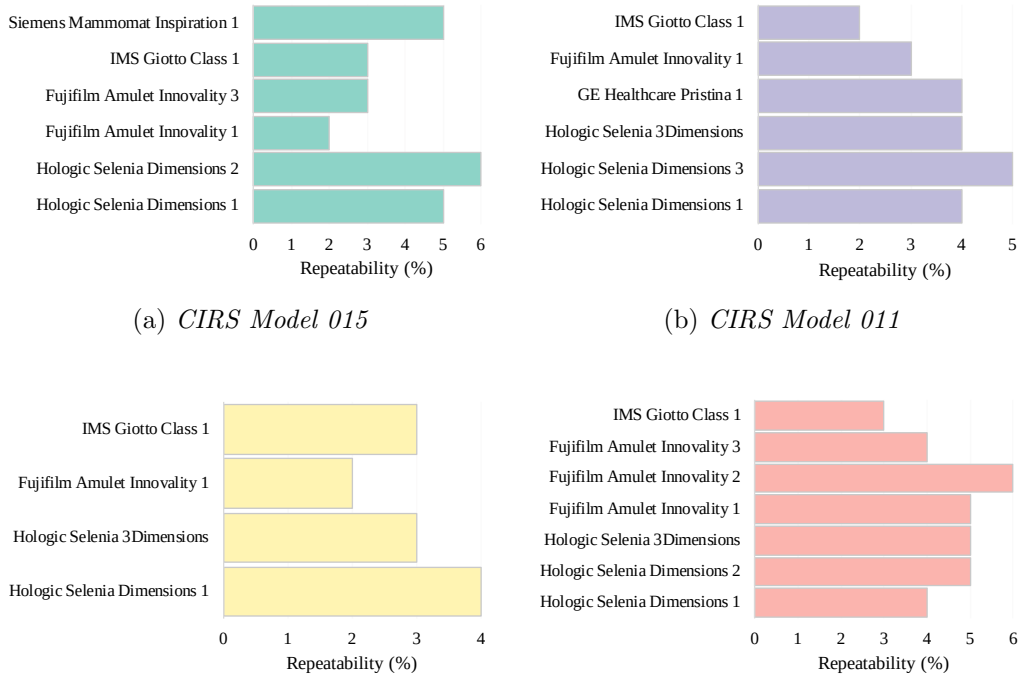

(a) *CIRS Model 015*

(b) *CIRS Model 011*

(c) *Modular DBT Phantom*

(d) *Tomophan*

Figure 5.5: Repeatability of the measurements in different DBT systems. Small values correspond to better repeatability.

From the analysis of the values reported in the previous figure it is possible to conclude that the repeatability, regardless of phantom type and mammography system, is always within 10%. According to this if, for a given DBT system-phantom configuration, only one exposure is available, an uncertainty equal to its 10% can be associated to the relative FWHM value.

5.3 Z-resolution

In this section, the experimental FWHM values of the ASF profiles obtained for the chosen details will be presented. Specifically, the results are reported separately for each phantom used.

CIRS Model 015
For the analysis of the z-resolution, the group of specks with a diameter of 0.32 mm, circled in red in Fig. 4.1a, was chosen so as to have similar detail sizes among the various phantoms. The following table summarizes the number of DBT systems, from different hospital facilities, used to experimentally acquire images of this phantom.

Mammography system	**CIRS 015**
GE Healthcare SenoClaire	1
GE Healthcare Pristina	4
Hologic Selenia Dimensions	5
Hologic 3Dimensions	-
IMS Giotto Class	2
Siemens Mammomat Inspiration	1
Siemens Mammomat Revelation	1
Fujifilm Amulet Innovality (FBP)	2

Table 5.1: Number of DBT systems tested to expose the CIRS model 015.

The experimental normalized ASF profiles, computed according to Eq. 4.1, are reported in Fig. 5.6 which gives a representative example for each DBT system tested. In detail, the figure shows overlapping ASF profiles in all cases where there are two different models of the same company, with the exception of the Fujifilm Amulet Innovality case where the different profiles are related to the two possible acquisition modes, namely ST and HR (see

Tab. 2.1), which differ in the width of the acquisition angle. Both the Innovality mammography systems used to expose this phantom implement a reconstruction algorithm based on the FBP method.
In the ASF profiles shown it can be seen that, regardless of the type of DBT system, the peak is always defined near the reconstructed slice number 37. This reflects the actual height (see Tab. 4.1) at which the details are located in the phantom. The reason why the peak does not always fall exactly at the height of the details, with respect to the breast support table, is related to the fact that the number of reconstructed slices is determined by the displayed thickness, possibly augmented by a variable number of additional planes that depends on the type of reconstruction algorithm implemented and thus on the DBT system model. These observations also apply to all the phantoms that will be described below. The reconstruction algorithms clearly influence the shape of the ASF profile, which appears different among the various models. In Fig. 5.6a, 5.6d, it can be seen that the different systems from the same company are very similar to each other, in terms of signal spread, and this is further confirmed by the respective numerical values of FWHM calculated. The Tab. 5.2, shown below, presents the characteristic FWHM values obtained for each type of DBT system tested.

Mammography system	**FWHM (mm)**
GE Healthcare SenoClaire	1.8 ± 0.2
GE Healthcare Pristina	2.0 ± 0.1
Hologic Selenia Dimensions	2.9 ± 0.1
Hologic 3Dimensions	-
IMS Giotto Class	1.8 ± 0.1
Siemens Mammomat Inspiration	2.5 ± 0.1
Siemens Mammomat Revelation	2.3 ± 0.2
Fujifilm Amulet Innovality ST (FBP)	6.0 ± 0.2
Fujifilm Amulet Innovality HR (FBP)	2.2 ± 0.1

Table 5.2: FWHM values of the CIRS Model 015 specks (0.32 mm).

The systems GE Healthcare SenoClaire and Pristina, as well as the Siemens Mammomat Inspiration and Revelation, taking into account the relative uncertainties, have consistent FWHM values, as expected. The particular case of Fujifilm Amulet Innovality system clearly shows the dependence of the z-resolution on the acquisition angular range: varying the angle from 15°

(ST mode) to 40° (HR mode) empirically yields a marked improvement in the resolution along the z-axis for the same DBT system and reconstruction algorithm. This is because a wider angle allows for better sampling, which is reflected in a more detailed reconstruction of the signal and thus even in an improved resolution in the z-direction.

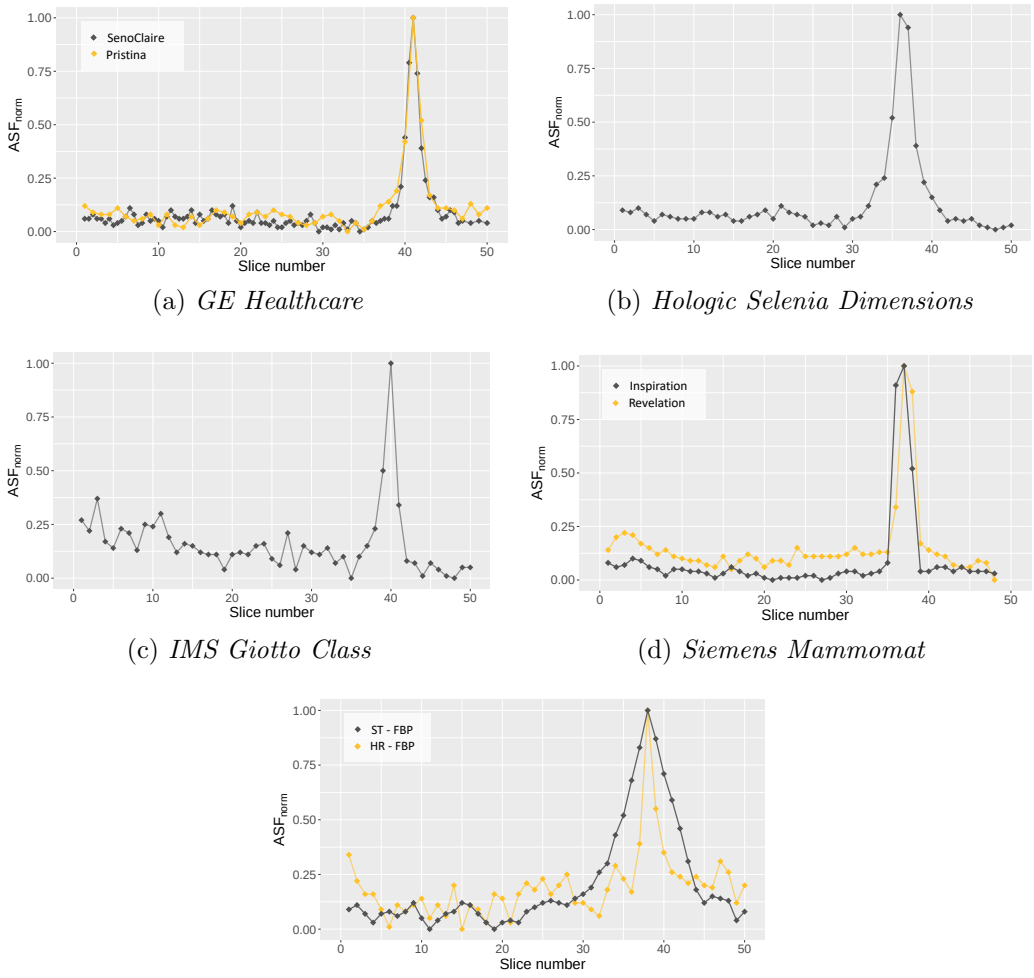

(a) *GE Healthcare*

(b) *Hologic Selenia Dimensions*

(c) *IMS Giotto Class*

(d) *Siemens Mammomat*

(e) *Fujifilm Amulet Innovality*

Figure 5.6: Experimental ASF profiles of the CIRS Model 015 specks.

CIRS Model 011

For the analysis of the z-resolution, the group of specks with a size of 0.40 mm, circled in red in Fig. 4.1b, was chosen. The following table summarizes the number of DBT systems, from different hospital facilities, used to experimentally acquire images of this phantom.

Mammography system	**CIRS 011**
GE Healthcare SenoClaire	-
GE Healthcare Pristina	2
Hologic Selenia Dimensions	6
Hologic 3Dimensions	1
IMS Giotto Class	1
Siemens Mammomat Inspiration	-
Siemens Mammomat Revelation	-
Fujifilm Amulet Innovality (FBP)	1
Fujifilm Amulet Innovality (Iterative)	1

Table 5.3: Number of DBT systems tested to expose the CIRS Model 011.

Mammography system	**FWHM (mm)**
GE Healthcare SenoClaire	-
GE Healthcare Pristina	2.9 ± 0.1
Hologic Selenia Dimensions	4.9 ± 0.1
Hologic 3Dimensions	5.2 ± 0.3
IMS Giotto Class	3.0 ± 0.1
Siemens Mammomat Inspiration	-
Siemens Mammomat Revelation	-
Fujifilm Amulet Innovality ST (FBP)	7.1 ± 0.3
Fujifilm Amulet Innovality ST (Iterative)	4.0 ± 0.4
Fujifilm Amulet Innovality HR (FBP)	2.5 ± 0.1
Fujifilm Amulet Innovality HR (Iterative)	2.0 ± 0.2

Table 5.4: FWHM values of the CIRS Model 011 specks (0.40 mm).

An example of the experimental normalized ASF profiles, for each DBT system experimentally tested, is shown below in Fig. 5.7. For the Fujifilm Amulet Innovality, the ASF profiles obtained from both empirically tested systems are presented separately for each acquisition mode. The reason is

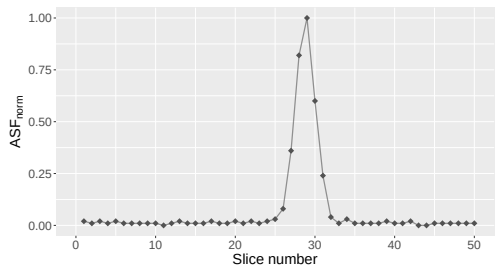

(a) *GE Healthcare Pristina*

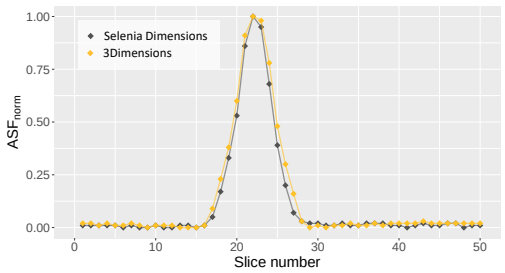

(b) *Hologic*

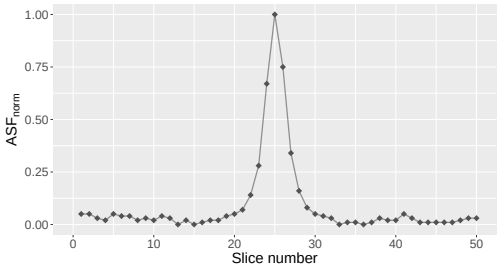

(c) *IMS Giotto Class*

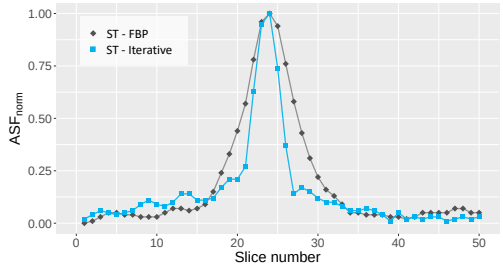

(d) *Fujifilm Amulet Innovality ST*

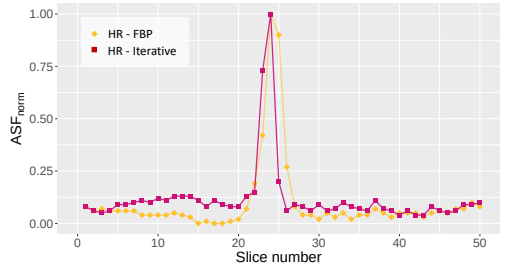

(e) *Fujifilm Amulet Innovality HR*

Figure 5.7: Experimental ASF profiles of the CIRS Model 011 specks.

that the two systems show different performance in terms of z-resolution and no typical response can be found. This is justified by the fact that one system is based on an iterative reconstruction while the other implements the FBP method. The influence of the reconstruction algorithm on the final results in terms of z-resolution was also observed in the previous case but now it is really evident. Notably, in this case the iterative approach provides systematically better results, as can be seen in Fig. 5.7d, 5.7e. The characteristic

values of FWHM obtained for this phantom, in each type of DBT system tested, are shown in Tab. 5.4. Again, the results of Fujifilm Amulet Innovality systems are presented separately according to the type of reconstruction algorithm implemented. In agreement with the calculated FWHM values shown in the table, the only available comparison between different models from the same company, Hologic, provides also in this case consistent results, a sign of comparable performance in terms of z-resolution (see Fig. 5.7b).

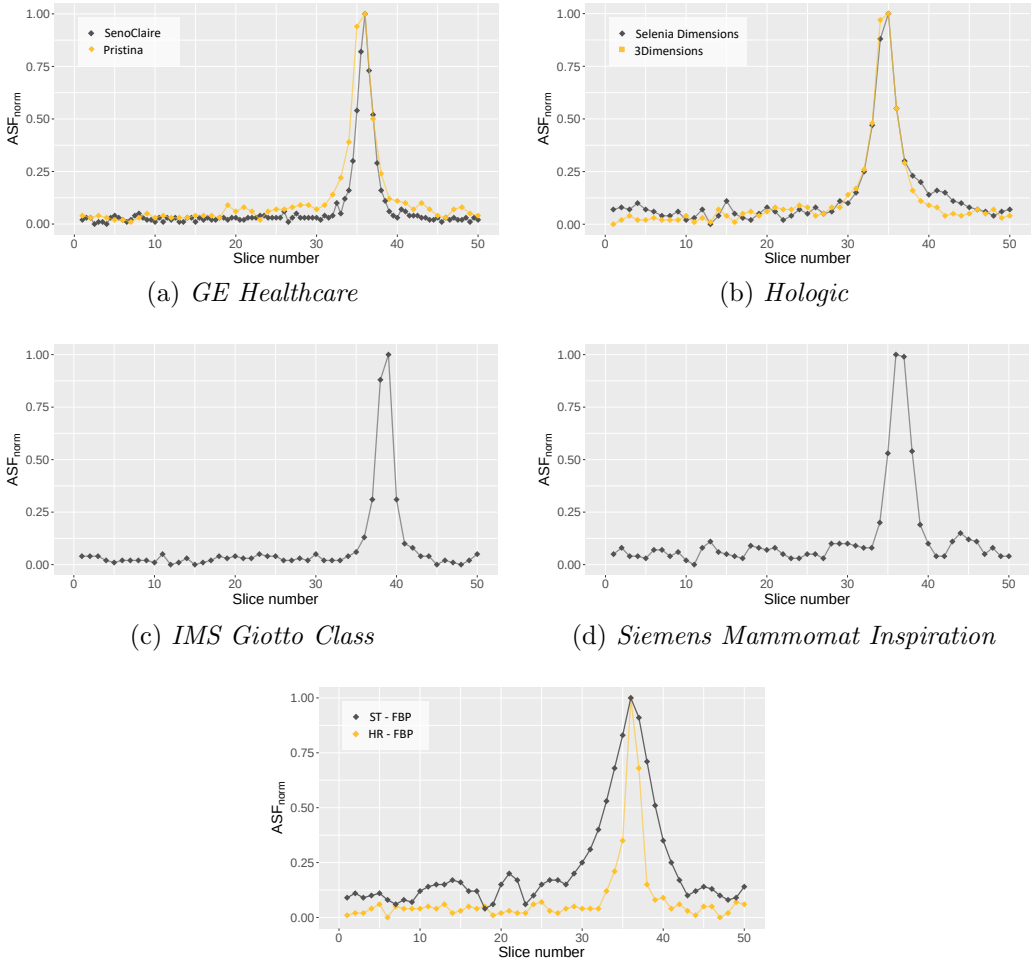

(a) *GE Healthcare*

(b) *Hologic*

(c) *IMS Giotto Class*

(d) *Siemens Mammomat Inspiration*

(e) *Fujifilm Amulet Innovality*

Figure 5.8: Experimental ASF profiles of the Modular specks.

Modular DBT Phantom

For the analysis of the z-resolution, the group of specks with a size of 0.33 mm, circled in red in Fig. 4.2a, was chosen. The following table summarizes the number of DBT systems, from different hospital facilities, used to experimentally acquire images of this phantom.

Mammography system	**Modular**
GE Healthcare SenoClaire	1
GE Healthcare Pristina	1
Hologic Selenia Dimensions	2
Hologic 3Dimensions	1
IMS Giotto Class	1
Siemens Mammomat Inspiration	1
Siemens Mammomat Revelation	-
Fujifilm Amulet Innovality (FBP)	1

Table 5.5: Number of systems tested to expose the Modular DBT Phantom.

The normalized ASF profiles, shown on the previous page in Fig. 5.8, which provides a representative example for each DBT system tested, are very similar to those found in the case of CIRS Model 015. In fact, the details analyzed are equivalent in terms of material and height, at which they are located in the phantom, and also have almost the same dimensions. For these reasons, similar results are expected in the characteristic FWHM values computed empirically in each DBT system. These are reported below in Tab. 5.6.

Mammography system	**FWHM (mm)**
GE Healthcare SenoClaire	2.1 ± 0.2
GE Healthcare Pristina	2.3 ± 0.2
Hologic Selenia Dimensions	3.1 ± 0.1
Hologic 3Dimensions	3.2 ± 0.1
IMS Giotto Class	2.1 ± 0.1
Siemens Mammomat Inspiration	3.2 ± 0.4
Siemens Mammomat Revelation	-
Fujifilm Amulet Innovality ST (FBP)	6.4 ± 0.2
Fujifilm Amulet Innovality HR (FBP)	2.3 ± 0.1

Table 5.6: FWHM values of the Modular DBT Phantom specks (0.33 mm).

The Fujifilm Amulet Innovality used to expose this phantom implements a reconstruction algorithm based on the FBP method. GE Healthcare's systems, as well as Hologic's, provide coherent FWHM values, respectively.

Tomophan
The number of DBT systems, from different hospital facilities, used to evaluate the z-resolution with this phantom are summarized below.

Mammography system	**Tomophan**
GE Healthcare SenoClaire	1
GE Healthcare Pristina	1
Hologic Selenia Dimensions	5
Hologic 3Dimensions	1
IMS Giotto Class	1
Siemens Mammomat Inspiration	1
Siemens Mammomat Revelation	1
Fujifilm Amulet Innovality (FBP)	3

Table 5.7: Number of DBT systems tested to expose the Tomophan.

The details of interest are three aluminum spheres of equal size, 0.50 mm, located at different heights from the base of the phantom, i.e. 18 mm, 28 mm, 38 mm. This can be clearly observed in the ASF profiles obtained, which present the signal spread of each sphere with the peak defined at the relative height. The Fig. 5.9 shows, as an example, the experimental normalized ASF profile of a single DBT system model for each company. The reason is that, as seen in all previous cases, the systems from the same vendor tested in this work are nearly equivalent from the point of view of the z-resolution. For the Fujifilm Amulet Innovality systems, all based on a FBP reconstruction algorithm, the profiles for ST and HR modes are shown separately.
For the first time, some DBT systems feature an ASF profile characterized by a plateau rather than a peak. These are specifically the Siemens Mammomat and Fujifilm Amulet Innovality systems. This peculiarity can be traced to the size and shape of the details. In fact, in this case, three-dimensional spheres are analyzed whereas all the phantoms described above feature smaller specks of known diameter but unknown shape. The phantom manuals do not specify in detail the geometry along the z-axis of the specks, which could therefore have a disk shape. In parallel, pure aluminum attenuates greatly compared

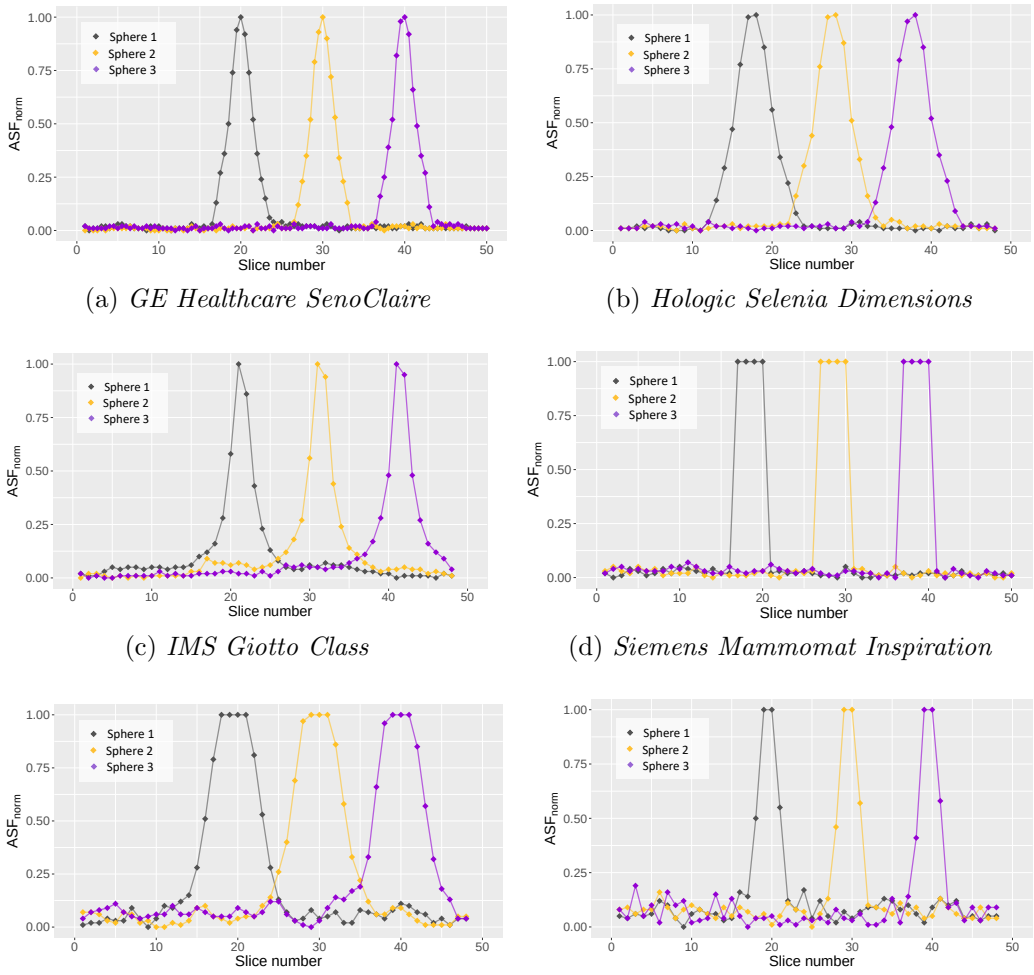

(a) *GE Healthcare SenoClaire*

(b) *Hologic Selenia Dimensions*

(c) *IMS Giotto Class*

(d) *Siemens Mammomat Inspiration*

(e) *Fujifilm Amulet Innovality ST*

(f) *Fujifilm Amulet Innovality HR*

Figure 5.9: Experimental ASF profiles of the Tomophan spheres.

with the background of the phantom, which mimics soft breast tissue, thus generating a very bright signal. The combination of these two factors means that, in some cases, the signal generated by the detail is reconstructed almost identically in the focal plane and those immediately adjacent to it. It is again evident that the final appearance of ASF profiles is determined primarily by the reconstruction algorithm implemented, since for the same detail, its shape varies greatly among different mammography system models.

Mammography system	FWHM (mm) h = 18 mm	h = 28 mm	h = 38 mm
GE Healthcare SenoClaire	3.2 ± 0.3	3.1 ± 0.3	3.1 ± 0.3
GE Healthcare Pristina	3.3 ± 0.3	3.2 ± 0.3	3.2 ± 0.3
Hologic Selenia Dimensions	5.1 ± 0.1	5.0 ± 0.2	5.0 ± 0.2
Hologic 3Dimensions	5.3 ± 0.4	5.1 ± 0.4	5.0 ± 0.3
IMS Giotto Class	3.1 ± 0.1	3.0 ± 0.3	3.0 ± 0.2
Siemens Mammomat Inspiration	4.1 ± 0.4	4.0 ± 0.4	4.0 ± 0.4
Siemens Mammomat Revelation	3.9 ± 0.4	3.9 ± 0.4	3.9 ± 0.4
Fujifilm Amulet Innovality ST (FBP)	6.9 ± 0.3	7.0 ± 0.3	7.0 ± 0.2
Fujifilm Amulet Innovality HR (FBP)	2.6 ± 0.1	2.6 ± 0.2	2.5 ± 0.1

Table 5.8: FWHM values of Tomophan spheres (0.50 mm) placed at different heights, i.e. 18 mm, 28 mm, 38 mm, relative to the base of the phantom.

The FWHM values of the three spheres, computed for the DBT systems, are reported in Tab. 5.8, shown above. A small dependence on detail height has been found in the literature [35, 39], for different DBT systems. However, the experimental results found in this thesis work show, for the three spheres, systematically consistent FWHM values, within the associated uncertainties. In order to evaluate the signal spread, regardless of the position of the detail along the z-axis, an equal reference height was defined for all the phantoms. Since the specks of the CIRS Modular 015 (non configurable phantom) and the highest sphere of the Tomophan are positioned at 37 mm and 38 mm relative to the base of the phantoms respectively, these values were chosen as reference. In detail, exploiting the modularity of the Modular DBT Phantom and Pixmam, two configurations described in *Section 4.1* were defined such that the details are placed at 37 mm. The only phantom that deviates from this general trend is the CIRS Modular 011, which is also non configurable, with the details at 23 mm above its base. For the Tomophan it is therefore possible to refer to the characteristic FWHM values given in the third column of Tab. 5.8.

Pixmam - 3D

For the z-resolution analysis three spheres, of 1.00 mm diameter, were chosen in the middle row, arranged orthogonally to the X-ray tube motion, which were in the useful field of view of all the DBT systems tested. These are

higlighted in red in Fig. 4.2c. The number of mammography systems, from different hospital facilities, used to acquire images of this phantom are summarized in the following table.

Mammography system	**Pixmam**
GE Healthcare SenoClaire	-
GE Healthcare Pristina	1
Hologic Selenia Dimensions	6
Hologic 3Dimensions	1
IMS Giotto Class	1
Siemens Mammomat Inspiration	1
Siemens Mammomat Revelation	1
Fujifilm Amulet Innovality (FBP)	2

Table 5.9: Number of DBT systems tested to expose Pixmam.

The normalized ASF profiles reported in Fig. 5.10, which provides a representative example for each DBT system tested, are similar but systematically wider than those found with the previous phantom. In fact, the type of detail analyzed and the material it is made of are the same but the Pixmam spheres are twice the size of the Tomophan spheres. This is also evident from the analysis of the calculated values of FWHM, reported in table below.

	FWHM (mm)		
Mammography system	**d = 6 cm**	**d = 11 cm**	**d = 16 cm**
GE Healthcare SenoClaire	-	-	-
GE Healthcare Pristina	6.0 ± 0.4	6.0 ± 0.3	5.6 ± 0.4
Hologic Selenia Dimensions	9.8 ± 0.2	9.8 ± 0.2	9.7 ± 0.2
Hologic 3Dimensions	9.9 ± 0.2	9.8 ± 0.3	9.7 ± 0.3
IMS Giotto Class	5.4 ± 0.4	5.2 ± 0.5	5.5 ± 0.4
Siemens Mammomat Inspiration	6.8 ± 0.6	6.7 ± 0.6	6.9 ± 0.7
Siemens Mammomat Revelation	6.9 ± 0.6	6.6 ± 0.6	6.8 ± 0.6
Fujifilm Amulet Innovality ST (FBP)	10.4 ± 0.4	10.2 ± 0.3	10.1 ± 0.5
Fujifilm Amulet Innovality HR (FBP)	4.3 ± 0.4	4.2 ± 0.3	4.2 ± 0.4

Table 5.10: FWHM values of Pixmam spheres (1.00 mm) placed at different distances, i.e. 6 cm, 11 cm, 16 cm, from the chest wall side.

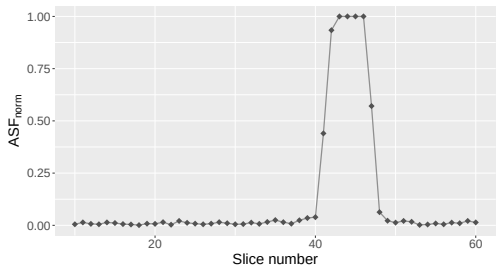

(a) *GE Healthcare Pristina*

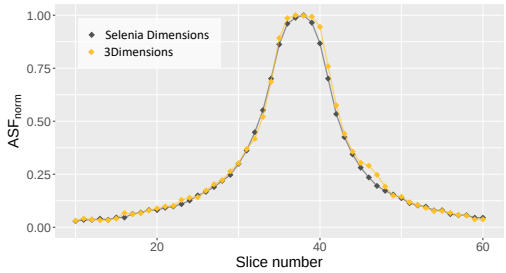

(b) *Hologic*

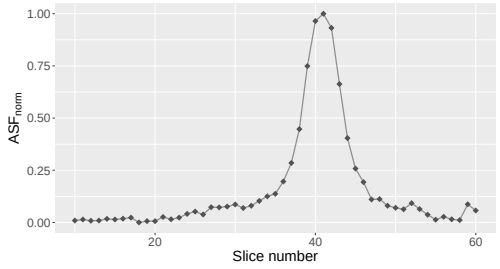

(c) *IMS Giotto Class*

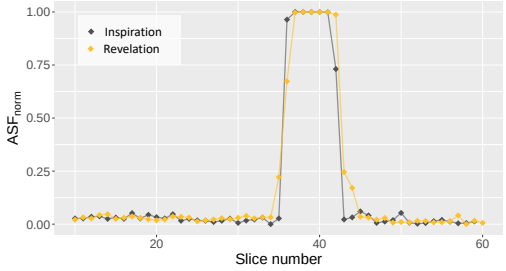

(d) *Siemens Mammomat*

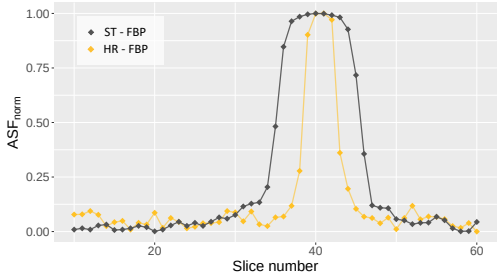

(e) *Fujifilm Amulet Innovality*

Figure 5.10: Experimental ASF profiles of the Pixmam spheres.

The Tab. 5.10 shows, for all the DBT systems, the FWHM values obtained for the three spheres placed at different distances, i.e. 6 cm, 11 cm, 16 cm, from the chest wall side. The results found are consistent for the three details, within the associated uncertainties, although a very slight dependence can be observed in the mean values but no general trend is identified among the different systems. The specific evaluation of the ASF as a function of sphere position on the plane, for each DBT system model, is beyond the scope of this work. Nevertheless Rodriguez-Ruiz, et al. [33] addressed this

issue demonstrating that details closer to chest wall sistematically provide more reproducible results. In addition, the positions closer to the chest are more interesting clinically since they correspond with high probability to the areas occupied by the patient's breasts. For the Tomophan it is therefore possible to refer to the FWHM values given in the first column of Tab. 5.10. The two Fujifilm Amulet Innovality systems used to expose this phantom both implement a reconstruction algorithm based on the FBP method.

5.4 Discussion

The experimental results presented above show that the z-resolution, quantified numerically through the FWHM value of the ASF profile obtained for a detail of interest, depends on several factors, namely the type of reconstruction algorithm implemented in the DBT system, the width of the acquisition angle and the characteristics of the detail.
The ASF profiles of the CIRS Model 015 (Fig. 5.6) and Modular DBT Phantom (Fig. 5.8), characterized by 0.32 mm and 0.33 mm details respectively, appear more affected by noise than the other phantoms, regardless of the type of mammography system. This effect may be related to the small size of the specks which generate lower PV than larger details. Thus their signal is more easily affected by variations in the background and the renormalization process of the signal spread, among the reconstructed slices, highlights this aspect. In fact, the ASF profiles of CIRS Model 011 (Fig. 5.7), characterized by 0.40 mm specks, already appear much less affected by noise. As expected, the size of the detail positively influences the signal reconstruction, in fact, a less noisy z-resolution response was empirically observed. However, it is crucial to note that noise mainly affects the ASF profile tails, so the evaluation of the FWHM is not particularly affected and is reliable even with very small details, such as specks.
The width of the experimental ASF profiles, and consequently the FWHM values found, show a dependence on the size of the detail. For example, with regard to specks, it can be observed that for a given DBT system the FWHM value obtained with the CIRS Model 015 (Tab. 5.2) is systematically smaller, but consistent with the corresponding value in the case of Modular DBT Phantom (Tab. 5.6). This is in agreement with the fact that the analyzed details are equivalent in terms of material and height relative to the base of the phantom and that their dimensions are almost the same, differ-

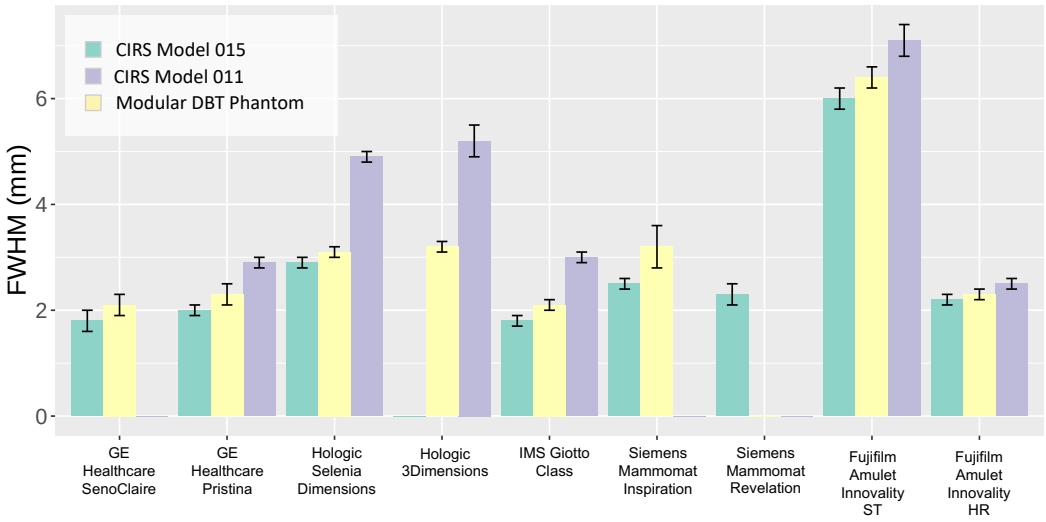

Figure 5.11: Characteristic FWHM values, of the various DBT systems experimentally found in phantoms with specks, namely CIRS Model 015 (0.32 mm), CIRS Model 011 (0.40 mm) and Modular DBT Phantom (0.33 mm).

ing by 0.01 mm. The Siemens Mammomat Inspiration provides, as expected, similar results for the two phantoms which, however, deviate more from each other than found in the other DBT systems. This could be due to a greater sensitivity to detail size of the Siemens Mammomat Inspiration or it could be related to the fact that, in both phantoms, the reported values were obtained from acquisitions on a single system from different hospital facilities. Therefore, it is very likely that the results reflect the peculiarities of a tested system, so it would be useful to increase the statistics. The characteristic FWHM values found with the CIRS Model 011 are larger than those found with the phantoms described above, in each DBT system tested. This is in agreement with the fact that CIRS Model 011 has the largest details, i.e. 0.40 mm. The general comparison of the FWHM values found for the three phantoms having groups of specks of different sizes is visible in Fig. 5.11, where all the experimental results and their uncertainties are represented. Specifically, in the CIRS Model 011 phantom, for the Fujifilm Amulet Innovality system, only the results obtained with the FBP reconstruction algorithm are reported for consistency. From the figure shown above, it is evident that as the size of the specks becomes bigger, the value of FWHM increases, as expected from literature [14, 34]. This suggests that the thickness of the specks

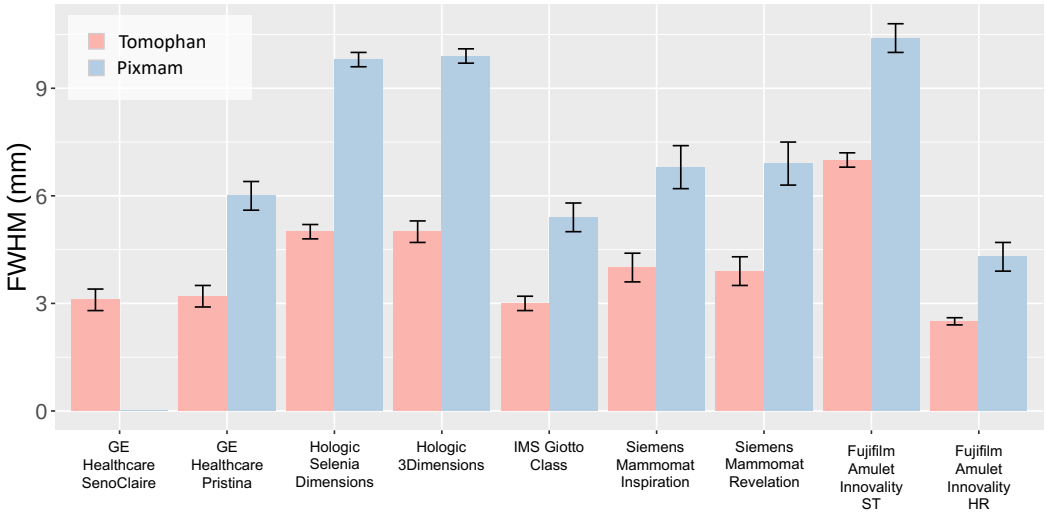

Figure 5.12: Characteristic FWHM values, of the various DBT systems, experimentally found in phantoms with spheres, namely Tomophan (0.50 mm) and Pixmam (1.00 mm).

along the z-axis, which is not known a priori, also increases along with the diameter defined in the x-y plane.
The dependence of the signal spread on the size of the details is observed empirically also with spheres. In particular, Pixmam details (1.00 mm) are twice as large as Tomophan details (0.50 mm), and this relationship is also evident in the numerical results, as expected. In fact, the values of FWHM calculated with Pixmam (Tab. 5.10) turn out to be double the corresponding values derived with Tomophan (Tab. 5.8), taking into account the associated uncertainties. The only exception is the Fujifilm Amulet Innovality system which, given the same reconstruction algorithm based on the FBP method, does not show a direct correlation between the detail size and the signal spread. The general comparison of the FWHM values found for the two phantoms having spheres of different sizes is visible in Fig. 5.12, where all the experimental results and their uncertainties are represented.
Interestingly, in the case of CIRS Model 011 and Tomophan, consistent FWHM values were always obtained despite the different detail sizes (Fig. 5.13), i.e. 0.40 mm for the former phantom and 0.50 mm for the latter. This could be attributed to several factors such as, the height, the material and shape of the details. The specks are located at 23 mm from the base

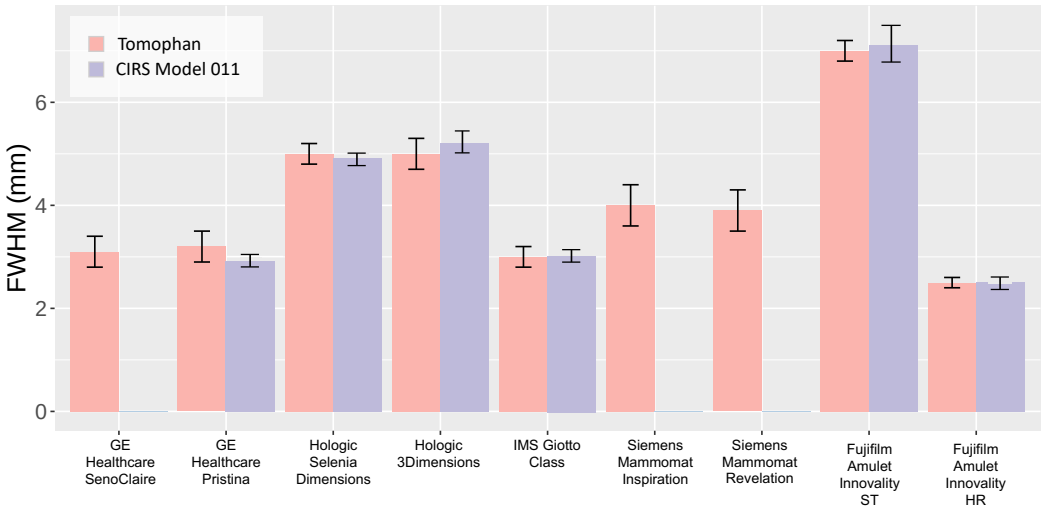

Figure 5.13: Characteristic FWHM values, of the various DBT systems, experimentally found in CIRS Modular 011 ($CaCO_3$ specks of 0.40 mm) and Tomophan (Al sphere of 0.50 mm).

of their phantom, while the sphere is positioned at 38 mm. This may influence the evaluation of the signal spread, as suggested in the literature [35, 39], although the experimental observations of the Tomophan results do not suggest a clear dependence of the FWHM on the analyzed height. The two details are also characterized by different materials, the specks being made of calcium carbonate, while the sphere of aluminum. The latter have the same density, ρ_{CaCO_3}=2.71 g/cm^3 and ρ_{Al}=2.70 g/cm^3, so in principle no different behavior is expected with respect to X-ray attenuation. Thus, the spread of the signal may be influenced by the different shape of the details along the z-axis, known in the case of spheres and unknown in the case of specks. From the experimental results, it can be assumed that the CIRS Model 011 details have a dimension in z similar to the diameter of the Tomophan sphere.
In light of the results obtained, it is possible to say that although only spheres are dedicated details for the z-resolution evaluation, groups of specks can also provide reliable results and seem to be a viable alternative, as suggested by [19]. In fact even the latter, as well as the spheres, are very small details contained entirely in a reconstructed focal plane. Furthermore they have the advantage of being more similar to the typical breast structures which is fundamental to reveal in the clinic for an early diagnosis.

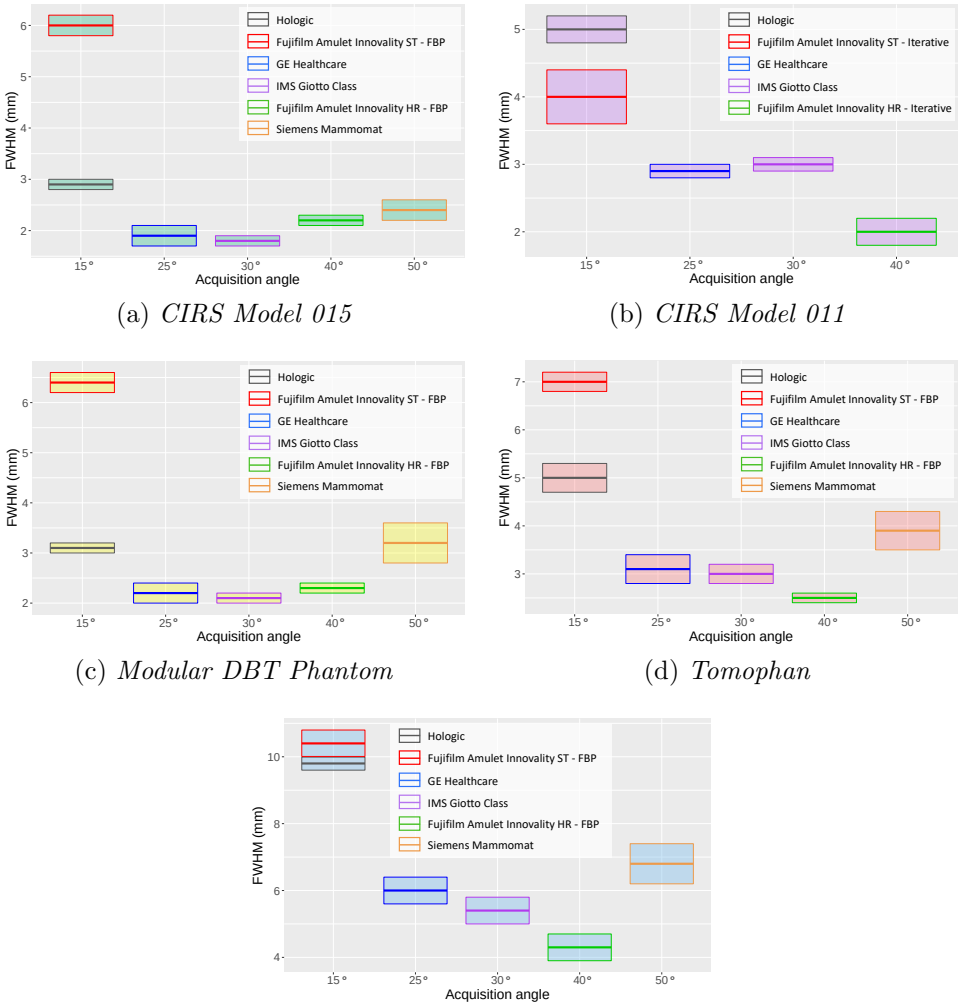

(a) *CIRS Model 015*

(b) *CIRS Model 011*

(c) *Modular DBT Phantom*

(d) *Tomophan*

(e) *Pixmam*

Figure 5.14: Dependence of the empirical FWHM values on the acquisition angular ranges of the various DBT system.

Among the various DBT systems tested, the Fujifilm Amulet Innovality allowed to directly observe the influence of the type of reconstruction algorithm and the acquisition angle on the z-resolution. The evaluation of the ASF profiles in the CIRS Model 011 phantom showed that the iterative image reconstruction provides significantly better results than the FBP method (Fig. 5.7d, 5.7e). In parallel, for the same reconstruction algorithm and re-

gardless of phantom type, the wider acquisition angle of the HR mode (40°) systematically improves the resolution compared with the ST mode (15°). It is known that the relatively poor spatial resolution along the z-axis, typical of tomosynthesis, is due to the limited angular range of acquisition. Therefore, smaller FWHM values were expected in correspondence of wider angles [14,29-32]. However, if the dependence of the resolution in the z-direction as a function of the acquisition angle is studied globally, taking into account all the DBT systems tested, the expected trend is not obtained. In fact in Fig. 5.14, which shows the characteristic FWHM values found with the associated uncertainties, no progressive improvement is observed in any phantom, as the scan angle increases. In detail, the results of the systems from the same company were merged because in all previous analyses it has been shown that their performance, in terms of z-resolution, are almost equivalent. Moreover, they are always characterized exactly by the same angular range of acquisition (Tab. 2.1). In 5.14b, only the results of the iterative Fujifilm Amulet Innovality system are reported in order to have a comparison of similar recostruction algorithms. From the experimental findings it is possible to deduce that the z-resolution is not influenced only by the acquisition angle but it is the results of the combination of several factors, the most crucial of which seems to be the type of reconstruction algorithm implemented. To date, the algorithms are almost all iterative, but each company has developed its own. In support of what has been said so far it is experimentally observed that the ASF profiles of the same company's DBT models, for a given phantom, are almost identical in all the cases analyzed, while appear different among DBT systems of various models.

It is interesting to compare the characteristic FWHM values found in this thesis work with known results in the literature. The comparison will be made considering only the Pixmam phantom because almost all studies refer to spheres of 1 mm. The reason is historical, as the first published DBT quality control protocol, EUREF 2013 [17], proposed only this type of detail to perform image quality QC test. In Tab. 5.11 are shown, for each DBT system, the values obtained in this work and those reported by the National Health Service (NHS) [37-44], Rodríguez-Ruiz et al. [33], Sundell et al. [35] and Sage et al. [36]. The Pixmam analysis yielded similar results to the NHS technical evaluations, as for some DBT systems the FWHM values are consistent, taking into account the relative uncertainties. The other known studies in the literature, however, do not agree with what was found in this thesis work. The main reason might be related to the different way in which

	FWHM (mm)				
Mammography system	**Thesis**	**NHS**	**Ruiz**	**Sundell**	**Sage**
GE Healthcare SenoClaire	-	6.0 (5.6-6.5)	-	7.4 ± 0.1	-
GE Healthcare Pristina	6.0 ± 0.4	7.9 (6.3-14)	-	-	7.8
Hologic Selenia Dimensions	9.8 ± 0.2	11 (9.9-12.2)	8.7	8.7 ± 0.1	8.6
Hologic 3Dimensions	9.9 ± 0.2	11 (10.5-11.3)	-	-	-
IMS Giotto Class	5.4 ± 0.4	5.8 (5.5-6.2)	-	-	-
Siemens Mammomat Inspiration	6.8 ± 0.6	7.1 (6.1-9.2)	3.7	-	5.2
Siemens Mammomat Revelation	6.9 ± 0.6	6.8 (6.4-7)	-	-	-
Fujifilm Amulet Innovality ST	10.4 ± 0.4	7.5 (6.7-8.8)	11	9.4 ± 0.1	-
Fujifilm Amulet Innovality HR	4.3 ± 0.4	2.8 (2.4-4.7)	4	3.5 ± 0.1	-

Table 5.11: Comparison of FWHM values of 1 mm spheres found in this thesis work and in the literature [33, 35-44].

the signal spread is calculated. In fact, as mentioned in *Section 3.5*, there are different mathematical expressions to define the ASF. In this thesis, and also in NHS evaluations, the maximum PV [19] is considered for the signal, while all the other studies take into account the mean PV [14, 33]. In parallel, there are several other factors that can invalidate the comparison of the measurements. The most trivial ones involve possible differences between the phantoms used that contain the 1 mm spheres, such as the height at which the details are placed, the material of the detail and that of the background. Another important factor that complicates the final comparison is the reconstruction algorithm implemented in the systems, given their rapid development nowadays (also in the form of software updates to existing configurations).

5.5 Limitations and future works

In light of the results obtained, it should not be forgotten that the study was conducted with small samples of experimental measurements. Therefore, although the results are consistent with each other and it is possible to identify, for the 5 phantoms, reference values for the systems tested, it is necessary to increase the statistics in order to define more reliable quantities, that can possibly be included in a protocol as typical values for the z-resolution QC test. In addition, it is desirable to improve the procedure by

which the FWHM is determined by developing, for example, an automated image analysis process and an optimized approach based on the specific characteristics of each phantom and/or mammography system.
This thesis work focuses on the z-resolution which, in digital breast tomosynthesis, is a single aspect of image quality, that includes also the evaluation of details visibility and homogeneity in the x-y plane. In the future it will be then possible to use all the images acquired so far to define procedures by which image quality can be assessed entirely by analyzing all types of details in the phantoms, i.e. fibers, low-contrast masses, microcalcifications, etc.

Conclusions

In Digital Breast Tomosynthesis (DBT), the assessment of image quality is a much-discussed topic. Understanding how to quantitatively interpret the visibility and representation quality of details in reconstructed images is a very difficult challenge involving many working groups of experts [20-23].
In this thesis work, one aspect of image quality, the z-resolution, was experimentally evaluated. The latter was studied in terms of ASF, a function that describes the signal spread of a detail along the reconstructed focal planes. To quantify the ASF numerically, its FWHM was calculated and used as a representative index of the z-resolution. In detail, measurements were acquired in 24 DBT systems currently in use in 20 hospital facilities in Italy. All the 7 mammography models present, to date, in public hospitals in our country were included in the study. The analysis was performed on clinical reconstructed DBT images of 5 different commercial phantoms, characterized by small details (0.32 mm - 1.00 mm), suitable for resolution assessment along the z-axis.
The possibility of having more than one experimental acquisition, for most of the systems, allowed to conclude that the repeatability of the measurements is good, always being within 10%. The analysis of the images led to the identification of characteristic FWHM values for each type of DBT system and phantom tested. The signal spread showed a dependence, known in the literature [14, 34], on the size of the detail analyzed. As the diameter of the speck/sphere increases, there is a systematic increase in the FWHM value, representing a more significant signal diffusion in the unfocused reconstructed planes. The experimental results showed that specks provide similar responses to spheres, thus appearing to be a viable alternative to them for evaluating the z-resolution, as suggested by [19]. The analysis of the ASF in Tomophan and Pixmam spheres allowed to study the influence of height and spatial position of the detail, respectively. In both phantoms, consistent

FWHM values were obtained for the considered details, so no explicit dependence on either the height, relative to the base of the phantom, or the spatial position, in the x-y plane, was evident in this work. Among the various systems tested, the Fujifilm Amulet Innovality allowed to directly observe the influence of the type of reconstruction algorithm and the acquisition angle on the z-resolution. The evaluation of the ASF in the CIRS Model 011 showed that the iterative image reconstruction provides significantly better results than the FBP method. In parallel, for the same reconstruction algorithm and regardless of phantom type, the wider acquisition angle of the HR mode (40°) systematically improves the resolution compared with the ST mode (15°), as expected in the literature [14,29-32]. If the dependence of the ASF on the acquisition angle is studied globally, considering all the various DBT systems tested, the expected trend is not observed. In fact, there is no progressive improvement in the z-resolution as the angle increases. This could be due to the fact that the final output results are obtained from the combination of several factors, the most crucial of which seems to be the type of reconstruction algorithm implemented. To date, the algorithms are almost all iterative, but each company has developed its own. In fact, the ASF profiles of DBT systems of the same company, for a given detail, are almost identical in all the cases analyzed, while appear different among various companies.
The characteristic FWHM values found in this thesis work of IMS Giotto Class, Siemens Mammomat Inspiration and Siemens Mammomat Revelation systems, for a 1 mm diameter spheres, yielded coherent results with the technical evaluations of the National Health Service (NHS) [41-43]. In contrast, the GE Healthcare Pristina and Fujifilm Amulet Innovality HR systems provided only similar results [37, 44]. The discrepancies in the other systems may be due to the different reconstruction algorithms implemented, as their rapid development complicates the ultimate comparison between studies.
The experimental approach shown in this thesis work can be proposed as a procedure for the z-resolution quality control test. The characteristic FWHM values experimentally obtained, for each DBT system-phantom configuration, could be used as a starting point to identify typical values of the z-resolution to be included as a reference in a quality control protocol for digital breast tomosynthesis. Clearly, to do this, it is necessary to acquire a statistically significant number of images for each model of DBT system. In this project, the equipment involved is located in hospital facilities in our country and is not available for research purposes. For this reason, only a limited amount of data was acquired and processed.

References

1. ICRP, 103. "The 2007 Recommendations of the International Commission on Radiological Protection". ICRP Publication 103 (2007).

2. Legislative Decree No. 101 implementing Directive 2013/59/Euratom – "Attuazione Della Direttiva 2013/59/Euratom, che Stabilisce Norme Fondamentali di Sicurezza Relative Alla Protezione Contro i Pericoli Derivanti dall'esposizione alle Radiazioni Ionizzanti, e che Abroga le Direttive 89/618/Euratom, 90/641/Euratom, 96/29/Euratom, 97/43/Euratom e 2003/122/Euratom e riordino della Normativa di Settore in Attuazione dell'Articolo 20, comma 1, lettera a), della legge 4 ottobre 2019, n. 117". Gazzetta Ufficiale della Repubblica Italiana: Roma, Italy (2020).

3. ISTISAN report - "Diagnostic reference levels for national practice of diagnostic and interventional radiology and of diagnostic nuclear medicine. Update of ISTISAN report 17/33 (2020/2022)".

4. Italian Association of Medical Oncology (AIOM). "I Numeri del Cancro in Italia", (2020).

5. Italian Association of Medical Oncology (AIOM). "I Numeri del Cancro in Italia", (2021).

6. Italian Cancer Registries Association (AIRTUM) "Ancora in calo la mortalità per tumore della mammella", XIV national meeting (2010).

7. Jesinger, Robert A. "Breast anatomy for the interventionalist." Techniques in vascular and interventional radiology 17.1 (2014).

8. Bernardi, Daniela, et al. "Digital breast tomosynthesis (dbt): recommendations from the italian college of breast radiologists (icbr) by the

italian society of medical radiology (sirm) and the italian group for mammography screening (gisma)." La radiologia medica, (2017).

9. Radiation Protection n° 162, "Criteria for Acceptability of Medical Radiological Equipment used in Diagnostic Radiology, Nuclear Medicine and Radiotherapy" (2012).

10. Ortenzia, O., et al. "Physical characterisation of four different commercial digital breast tomosynthesis systems." Radiation Protection Dosimetry 181.3 (2018).

11. IEC 62220-1 - "Medical electrical equipment - Characteristics of digital X-ray imaging devices - Part 1-1: Determination of the detective quantum efficiency - Detectors used in radiographic imaging", (2015).

12. Boone, John M., Thomas R. Fewell, and Robert J. Jennings. "Molybdenum, rhodium, and tungsten anode spectral models using interpolating polynomials with application to mammography." Medical physics 24.12 (1997).

13. DICOM Standards Committee, Digital Imaging and Communications in Medicine (DICOM). "Supplement 125: Breast Tomosynthesis Image Storage SOP Class", (2008).

14. Wu, Tao, et al. "A comparison of reconstruction algorithms for breast tomosynthesis." Medical physics 31.9 (2004).

15. Vedantham, Srinivasan, et al. "Digital breast tomosynthesis: state of the art." Radiology 277.3 (2015).

16. European Federation Of Organisations For Medical Physics (EFOMP) "Quality Controls in Digital Mammography - Protocol of the EFOMP Mammo Working group" (March 2015).

17. European Reference Organisation For Quality Assured Breast Screening And Diagnostic Services (EUREF) "European guidelines for quality assurance in breast cancer screening and diagnosis", Fourth edition-Supplements (2013).

18. European Reference Organisation For Quality Assured Breast Screening And Diagnostic Services (EUREF) “Protocol for the Quality Control of the Physical and Technical Aspects of Digital Breast Tomosynthesis Systems”, version 1.03 (March 2018).

19. American College Of Radiology (ACR) “Quality control manual 2D and Digital Breast Tomosynthesis”, Revised 2nd edition (May 2020).

20. EFOMP “Breast Tomosynthesis QC Protocol”, working group. Website: https://www.efomp.org/working-groups

21. Joint EFOMP-AAPM WG ”Breast dosimetry”, working group. Website: https://www.efomp.org/working-groups

22. AAPM COMMITTEE TREE, Task Group No. 245 - Tomosynthesis Quality Control (TG245). Website: aapm.org

23. AAPM COMMITTEE TREE, Task Group No. 323 - Development of a new breast dosimetry phantom (TG323). Website: aapm.org

24. Robson, K. J. ”A parametric method for determining mammographic x-ray tube output and half value layer.” The British Journal of Radiology 74:335-340 (2001).

25. Dance, D. R., et al. ”Additional factors for the estimation of mean glandular breast dose using the UK mammography dosimetry protocol.” Physics in medicine & biology 45.11-3225 (2000).

26. Dance, D. R. ”Monte-Carlo calculation of conversion factors for the estimation of mean glandular breast dose.” Physics in Medicine & Biology 35.9-1211 (1990).

27. Dance, D. R., K. C. Young, and R. E. Van Engen. ”Further factors for the estimation of mean glandular dose using the United Kingdom, European and IAEA breast dosimetry protocols.” Physics in Medicine & Biology 54.14-4361 (2009).

28. Dance, D. R., K. C. Young, and R. E. Van Engen. ”Estimation of mean glandular dose for breast tomosynthesis: factors for use with the UK, European and IAEA breast dosimetry protocols.” Physics in Medicine & Biology 56.2-453 (2010).

29. Zhao, Bo, and Wei Zhao. "Three-dimensional linear system analysis for breast tomosynthesis." Medical Physics 35.12 (2008).

30. Zhao, Bo, et al. "Experimental validation of a three-dimensional linear system model for breast tomosynthesis." Medical physics 36.1 (2009).

31. Hu YH, Zhao B, Zhao W. Artifacts in digital breast tomosynthesis: investigation of the effects of system geometry and reconstruction parameters using a linear system approach. Med Phys (2008).

32. Maki, Aili, et al. "Quality control of breast tomosynthesis for a screening trial: Preliminary experience." International Workshop on Breast Imaging. Springer, Cham, (2016).

33. Rodríguez-Ruiz, Alejandro, et al. "Evaluation of the technical performance of three different commercial digital breast tomosynthesis systems in the clinical environment." Physica Medica 32.6 (2016).

34. Maldera, A., et al. "Digital breast tomosynthesis: dose and image quality assessment." Physica Medica 33 (2017).

35. Sundell, Veli-Matti, et al. "A phantom study comparing technical image quality of five breast tomosynthesis systems." Physica Medica 63 (2019).

36. Sage, Julie, et al. "Experimental evaluation of seven quality control phantoms for digital breast tomosynthesis." Physica Medica 57 (2019).

37. Strudley CJ, Oduko JM, Young KC. Technical evaluation of GE Healthcare Pristina digital breast tomosynthesis system (NHSBSP Equipment Report). London: Public Health England (2019).

38. Strudley CJ, Oduko JM, Young KC. Technical evaluation of GE Healthcare SenoClaire digital breast tomosynthesis system (NHSBSP Equipment Report). London: Public Health England (2016).

39. Strudley CJ, Looney P, Young KC. Technical evaluation of Hologic Selenia Dimensions digital breast tomosynthesis system (NHSBSP Equipment Report 1307 Version 2). Sheffield: NHS Cancer Screening Programmes (2014).

40. Strudley CJ, Looney P, Young KC. Technical evaluation of Hologic 3Dimensions digital breast tomosynthesis system (NHSBSP Equipment Report). Sheffield: NHS Cancer Screening Programmes (2019).

41. Strudley CJ, Oduko JM, Young KC. Technical evaluation of IMS Giotto Class digital breast tomosynthesis system (NHSBSP Equipment Report). London: Public Health England (2018).

42. Strudley CJ, Warren LM, Young KC. Technical evaluation of Siemens Mammomat Inspiration digital breast tomosynthesis system (NHSBSP Equipment Report 1306 Version 2). Sheffield: NHS Cancer Screening Programmes (2018).

43. Strudley CJ, Warren LM, Young KC. Technical evaluation of Siemens Mammomat Revelation digital breast tomosynthesis system (NHSBSP Equipment Report). Sheffield: NHS Cancer Screening Programmes (2019).

44. Strudley CJ, Hadjipanteli A, Oduko JM, Young KC. Technical evaluation of Fujifilm AMULET Innovality digital breast tomosynthesis system (NHSBSP Equipment Report). London: Public Health England (2018).

Acknowledgements

I would like to thank the medical physicists of the AIFM Tomo Working Group working at the following hospital facilities,
AOU Città della salute e della scienza, Torino,
ASL BT, P.O. Dimiccoli, Barletta,
ASL CN1, Cuneo,
ASL2 Ospedale Santa Corona, Pietra Ligure (SV),
ASST dei Sette Laghi, Varese,
ASST Nord Milano,
ASUR Marche Area Vasta3, Macerata,
AUSL Romagna, Ravenna
Azienda AUSL IRCCS di Reggio Emilia,
Azienda Toscana Nord Ovest, Lucca,
Azienda USL Bologna,
Azienda USL Modena,
IEO Istituto Europeo di Oncologia, Milano,
IRCCS Ospedale San Raffaele - Gruppo San Donato, Milano,
San Giovanni Calibita - Fatebenefratelli - Isola Tiberina, Roma,
San Giuseppe, Empoli (FI),
Studio Associato Fisici Sanitari, Lugo (Ra),
for their contributions to the collection of data needed for this thesis work.